Special Issue Invited Review

Role of Ultrasound and Photoacoustic Imaging in Photodynamic Therapy for Cancer[†]

Scott C. Hester, Maju Kuriakose, Christopher D. Nguyen and Srivalleesha Mallidi* iD
Department of Biomedical Engineering, Tufts University, Medford, MA

ABSTRACT

Photodynamic therapy (PDT) is a phototoxic treatment with high spatial and temporal control and has shown tremendous promise in the management of cancer due to its high efficacy and minimal side effects. PDT efficacy is dictated by a complex relationship between dosimetry parameters such as the concentration of the photosensitizer at the tumor site, its spatial localization (intracellular or extracellular), light dose and distribution, oxygen distribution and concentration, and the heterogeneity of the inter- and intratumoral microenvironment. Studying and characterizing these parameters, along with monitoring tumor heterogeneity pre- and post-PDT, provides essential data for predicting therapeutic response and the design of subsequent therapies. In this review, we elucidate the role of ultrasound (US) and photoacoustic imaging in improving PDT-mediated outcomes in cancer—from tracking photosensitizer uptake and vascular destruction, to measuring oxygenation dynamics and the overall evaluation of tumor responses. We also present recent advances in multifunctional theranostic nanomaterials that can improve either US or photoacoustic imaging contrast, as well as deliver photosensitizers specifically to tumors. Given the wide availability, low-cost, portability and nonionizing nature of US and photoacoustic imaging, together with their capabilities of providing multiparametric morphological and functional information, these technologies are thusly inimitable when deployed in conjunction with PDT.

INTRODUCTION

About 1 in 6 human deaths are cancer-related, making it the second leading cause of death globally. The World Health Organization reported an estimated 9.6 million deaths due to cancer in 2018 alone (1). For decades, the surgical excision of tumors has been the mainstay of treatment, paired with or subsequently followed up with radiation and chemotherapy, both of which have severe side effects. A dedicated effort is underway to develop effective therapies that can be spatially and temporally localized to a tumor, with minimal damage to surrounding healthy tissue and low systemic toxicity. It would also be most advantageous for these novel therapies to possess minimal or nonoverlapping toxicity profiles when combined with other modes of therapy. Photodynamic therapy (PDT) is one such photochemistry-based modality that imparts preferential light-mediated cytotoxicity to target tissues while sparing surrounding healthy tissue, and is a technique that has shown tremendous potential for impacting and improving outcomes in cancer therapies (2).

PDT imparts cytotoxicity via the generation of reactive species by a photosensitizer (PS) molecule irradiated by a particular wavelength of light (Fig. 1). Specifically, the optically excited PS molecule in its triplet state interacts with either molecular oxygen (type-II PDT) in its vicinity to generate cytotoxic reactive oxygen species (ROS) or a microenvironmental substrate (type-I PDT) to generate reactive molecular species. The PDT field has grown by leaps and bounds since its first report by Raab *et al.* in 1990 (3), including the notable development of effective PSs with optical absorption maxima in the near-infrared (NIR) range (~600–800 nm). Greater understanding of cellular mechanisms of action and effects on immune response due to PDT have also been extensively studied (4). The field has burgeoned further due to two notable advantages of PDT for cancer therapy: (1) its spatial and temporal selectivity (5) and (2) its effectiveness on chemo- and drug-resistant cells (6–8). Preclinical studies have shown that PDT destroys tumor stroma and increases tumoral drug perfusion, making it an ideal complement to potent drugs that are otherwise unable to perfuse through stromal layers on their own (9–11). PDT has received regulatory approval for the treatment of several types of carcinoma and noncarcinoma pathologies, such as age-related macular degeneration (AMD). As a clinical example, PDT of pancreatic cancer increased survival time to 12.5 months from initial diagnosis, up from the typical median survival rates for this disease (6–10 months without metastases) (12–19). Moreover, in preclinical prostate, glioma and pancreatic cancer models, PDT has also shown a dose-dependent decrease in metastases (20–22). Despite its salient features and potential in various clinical studies, a key barrier for PDT success is its variability in treatment outcomes, which may be a direct result of either under- or overtreating of lesions. Accurate dosimetry determined from pretreatment tumor parameters, such as size, vascular density, oxygenation status, PS uptake and online or post-therapy monitoring, will expedite the widespread adoption of PDT technology.

Estimation of the deposited PDT dose and evaluation of the subsequent therapeutic response are a complex interdependence between the energy of delivered light, PS delivery efficiency, successful tumoral PS uptake and retention, PS clearance from the lesion, and the availability of oxygen in the treatment area (5,23–25). Direct dosimetry parameters such as PS photobleaching via fluorescence imaging and direct singlet oxygen measurement via luminescence at 1270 nm have been used previously to gauge deposited PDT dose (24–27). Either of these parameters individually or in combination were thought to be sufficient indicators of PDT dosage. However, it should be noted that these measurements are sampled at discrete locations in the tumor or are obtained from surface area-weighted fluorescence images. Research is being pursued by several groups to understand these dosimetry nuances further via the generation of 2D and 3D maps of surrogate markers such as tumor volume, vascular function and density, tumor blood oxygenation and tumor hypoxia status (5,28). Clinical positron emission tomography (PET), computed tomography (CT) and magnetic resonance imaging (MRI), while successful in providing data on tumor volumes, are limited by their lack of resolving power of microcirculatory activity without the use of exogenous contrast agents. There is a pressing need for imaging techniques that can monitor and assess changes in these surrogate dosimetry markers at various time points during therapy without the use of exogenous contrast agents in order to bolster treatment outcomes.

Among different clinical imaging modalities, ultrasound (US) is a ubiquitously available, nonionizing, low-cost, portable and real-time imaging technique that leverages the ability of acoustic waves to propagate deeply through tissues and scatter back to the receiver. It has become a primary method to measure structural and volumetric changes in tumors post-treatment. The variations in echogenicity or acoustic impedance of tumoral and healthy tissue are instrumental in demarcating their respective boundaries within an US image. Specifically, when acoustic wavefronts generated by a transducer bounce off of the target (termed backscatter) and return to a detecting transducer, a 2-dimensional image is generated from calculations of amplitude and the transmission-to-detection interval of the echo. Additional technologies, such as Doppler ultrasonography, can measure blood flow based on changes in frequency of the reflected sound wave from a moving object such as blood traveling through vessels. These unique features are primarily responsible for the prolific deployment of US imaging in both preclinical and clinical research settings. Traditional US imaging can provide information on tumor shape, size and vascular density (Fig. 1); however, it does not provide information on a tumor's oxygenation status. When US imaging systems are integrated with a nanosecond-pulsed laser, photoacoustic (PA) images of tissues (courtesy of acoustic wave generation via thermoelastic expansion due to light absorption by a chromophore such as hemoglobin) can be obtained utilizing the same US transmit/receiver probe (transducer), which has been demonstrated by us and others (28–33). PA imaging provides functional information by capitalizing on the wavelength-dependent optical absorption (μ_{abs}) profiles of the chromophores within the imaged region, which in the case of hemoglobin stems from whether it is oxygenated or deoxygenated (29,34,35). Both US and PA imaging utilize similar receiver electronics. Therefore, PA imaging can be transparently integrated with widely available US imaging devices (28,35,36), the combination of which can provide both structural and functional information at better resolutions than MRI or PET (albeit with less penetration depth, but sufficient to obtain 3D tumor data for many types of cancers) in a single system.

In this review, we showcase the current efforts in the field of US and PA imaging and discuss their role in improving PDT outcomes of cancer—from the planning stage to predicting treatment response without the use of exogenous contrast agents, to monitoring PS uptake and vascular destruction with the use of contrast agents. The PS is a theranostic molecule which can act
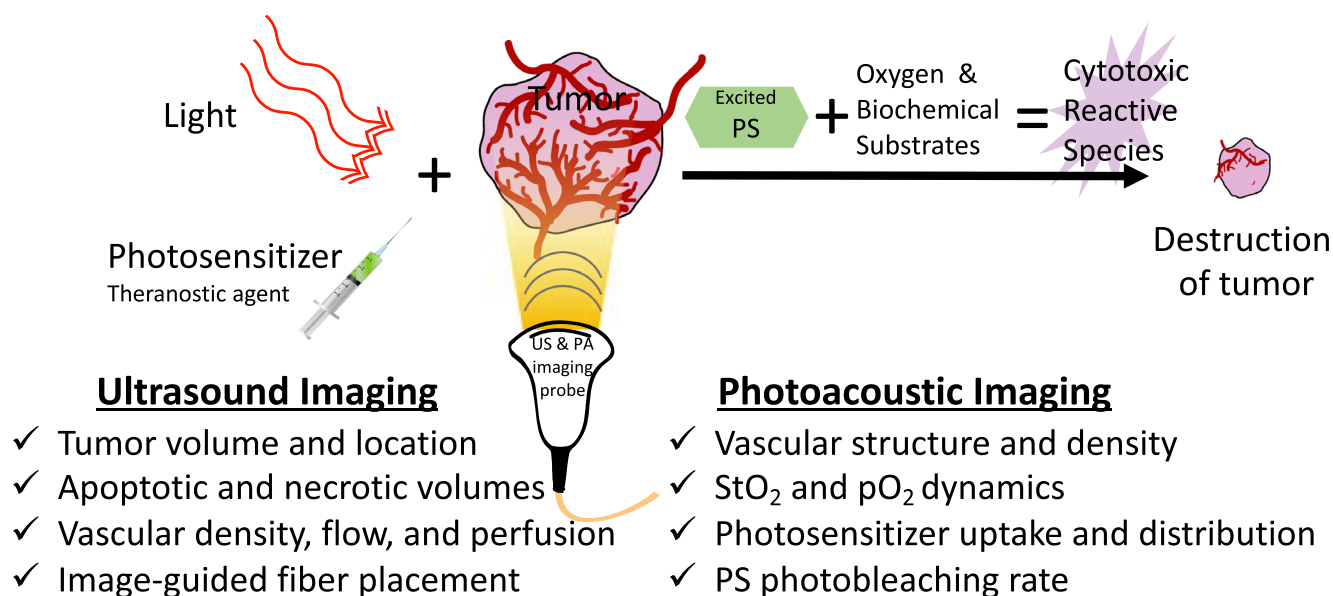

Figure 1. Schematic representation of PDT mechanism and list of ultrasound (US) and photoacoustic imaging surrogate markers obtained pre-, during and post-therapy. The photosensitizer (PS) is a phototoxic theranostic agent that upon light activation transitions into an excited triplet state and reacts with the surrounding environment (such as ground state molecular oxygen) to generate cytotoxic reactive species (such as singlet oxygen) leading to cell death. The bottom panel lists various structural and functional information that can be obtained with US and photoacoustic imaging to guide, monitor and assess PDT response. StO$_2$, blood oxygen saturation. pO$_2$, partial pressure of oxygen.

as an optical imaging contrast agent as well as a PDT agent. Multiwavelength or spectroscopic PA imaging confers the ability to visualize a multitude of chromophores with different optical absorption properties, whether they be exogenous and/or endogenous, via spectral unmixing (37). When delivered via nanoconstructs, PSs can act as PA contrast agents due to the high optical absorption of these carrier molecules compared to the surrounding tissue, thereby making it feasible to monitor PS uptake in the tumors. Based on whether nanoparticles were utilized to deliver PSs or exogenous contrast agents were employed to obtain surrogate imaging markers for PDT efficacy, this review is specifically divided into three parts: (1) role of US imaging in PDT, (2) role of PA imaging in PDT and (3) recent advances in multifunctional theranostic nanomaterials that can strengthen the photodynamic effect, enhance US and PA imaging contrast, and improve the precision of PS delivery to tumors, sometimes combinatorially.

ROLE OF US IMAGING IN PDT

Monitoring tumor structural and morphological changes due to PDT

Ultrasound is an established and cost-effective clinical method for identifying tumors and assessing disease progression via monitoring changes in tumor volume. Generally, cancerous tissues have different echogenicity when compared to healthy surrounding tissue structures, making their detection facile. Calculating the distance between two reflective boundaries is a common method for acquiring measurements of tumor diameters in all three (length, width and depth) spatial dimensions. Tumor volume is calculated with an ellipsoid volume formula $\pi/6 \times l$(ength) $\times$ w(idth) $\times$ d(epth); however, this method can either over- or underestimate native tumor volumes as tumors (clinical or preclinical) are not ellipsoid, particularly as they grow larger in size. From advances in 3D reconstruction software and computing power, US imaging now enables high-throughput acquisition and display of 3D volumetric maps of tumors. For example, in preclinical setting, accuracy of US-based volumetric measurements has been demonstrated by Pigula *et al.*, where they measured orthotopic pancreatic tumor volume with US imaging and found strong correlations with the gold standard of tumor weight and caliper-derived volume measurements of excised tumors (Fig. 2) (38). Furthermore, the study also revealed a tumor size-dependent response to PS benzoporphyrin derivative-based PDT. Small tumors (<35 mm^3) responded to a single round of PDT, while large tumors (>35 mm^3) showed no response to the same treatment, indicating PDT dose needs to be carefully determined based on pretreatment tumor volume (Fig. 2C). A clinical example that showcases the ability of US imaging to monitor PDT responses was presented by Moore *et al.*, where normal and basal cell carcinoma (BCC) thicknesses in 181 patients were monitored immediately before and up to a year after PDT (39). The study found that the thickness of BCC tumors were reduced by ~46% (i.e. 1.3 ± 0.8 mm to 0.6 ± 0.8 mm; P-value < 0.001) 4–6 weeks after the PDT regimen when compared to the pretreated tumors. Similar to the study by Pigula *et al.*, Moore *et al.* also found a tumor thickness-dependent response ratio following PDT, with thinner (diameter ≤ 1.5 mm) BCC lesions responding better to PDT (85% responded) than thicker (diameter ≤ 3 mm) lesions (75% responded). Given the high-throughput, contrast agent-free volumetric measurements provided by US imaging, strategic decisions on the timing of subsequent PDT or combination treatments can be designed and administered for maximal efficaciousness.

Beyond the detection of lesion boundaries and calculating tumor volume, US can also provide therapeutically relevant information on apoptotic cell death based on alterations in US backscatter intensity. Initially demonstrated by Banihashemi *et al.*, the spectral slope of the US backscattered signal is related to the size of the US scatterer, in their case the nucleus. As cells undergo apoptosis, the nucleus coalesces and condenses to a point of no return (termed pyknosis), and the cell membrane undergoes stochastic bulging and deformation (termed blebbing) which thusly affects the backscatter profiles of US waves that encounter it. Currently, invasive and time-consuming standard microscopy methods are utilized to evaluate cellular apoptosis. Given the real-time imaging capabilities of US imaging and its sensitivity to changes in nuclear size dynamics, quantitative US imaging techniques have been successfully used to monitor apoptosis in tumors due to PDT. Banihashemi *et al.* illustrated the monitoring of cell death following PDT in SCID mice harboring human melanoma HTB-67-induced tumors using a broadband and high-frequency US transducer (26 and 40 MHz central frequency), and showed a time-dependent increase in US backscatter which corresponded to tumor cell death during Photofrin-based PDT (110 J cm^{-2} light administered for 30 s) of subcutaneous tumors (40). Forty-eight hours post-PDT, they observed a decrease in US backscatter, which they attributed to the degradation of tumor nuclei. Multiple parameters derived from the spectroscopic analysis of the US backscatter frequency content were shown to correlate with tumor response early in the course of treatment by Czarnota *et al.* (40,41). From their work, an excellent visualization of variations in backscatter as a proxy for apoptosis can be seen in Fig. 3B. Based on these observations, Banihashemi *et al.* concluded that it provides a foundation for future investigations regarding the use of spectroscopic US imaging to monitor treatment and aid in the customization of treatments, particularly PDT. With availability of high-frequency US systems on catheters and endoscopic probes, spectroscopic US analysis could soon find its place to monitor PDT outcome for deeply situated tumors in both preclinical and clinical settings.

Acoustic frequency-dependent attenuation in tissues limits the applicability of US imaging to a few tens of centimeters. Moreover, an inverse relationship exists between penetration depth and central frequency of the transducer (thereby the spatial resolution). The higher the transducer frequency, the greater the spatial resolution, and the shallower the penetration depth. Higher frequency transducers (>20 MHz central frequency) are primarily used in preclinical settings to monitor tumor volume in small animal models such as the rodent models and are very limitedly utilized in clinical settings for ophthalmic or skin applications. In preclinical xenograft models, Ayers *et al.* have demonstrated that the volume of tumors measured via US is more accurate and requires ~30% fewer animals to reach statistical significance when compared to standard caliper measurements (42). In another study, Ramaswamy *et al.* demonstrated that low-field magnetic resonance imaging (MRI) and US imaging have similar accuracies in determining tumor volume and growth (43). Given the low-cost and high-throughput platforms that exist for 3D structural mapping, US imaging is primarily preferred for measuring most solid tumors aside from those of the brain or bone.
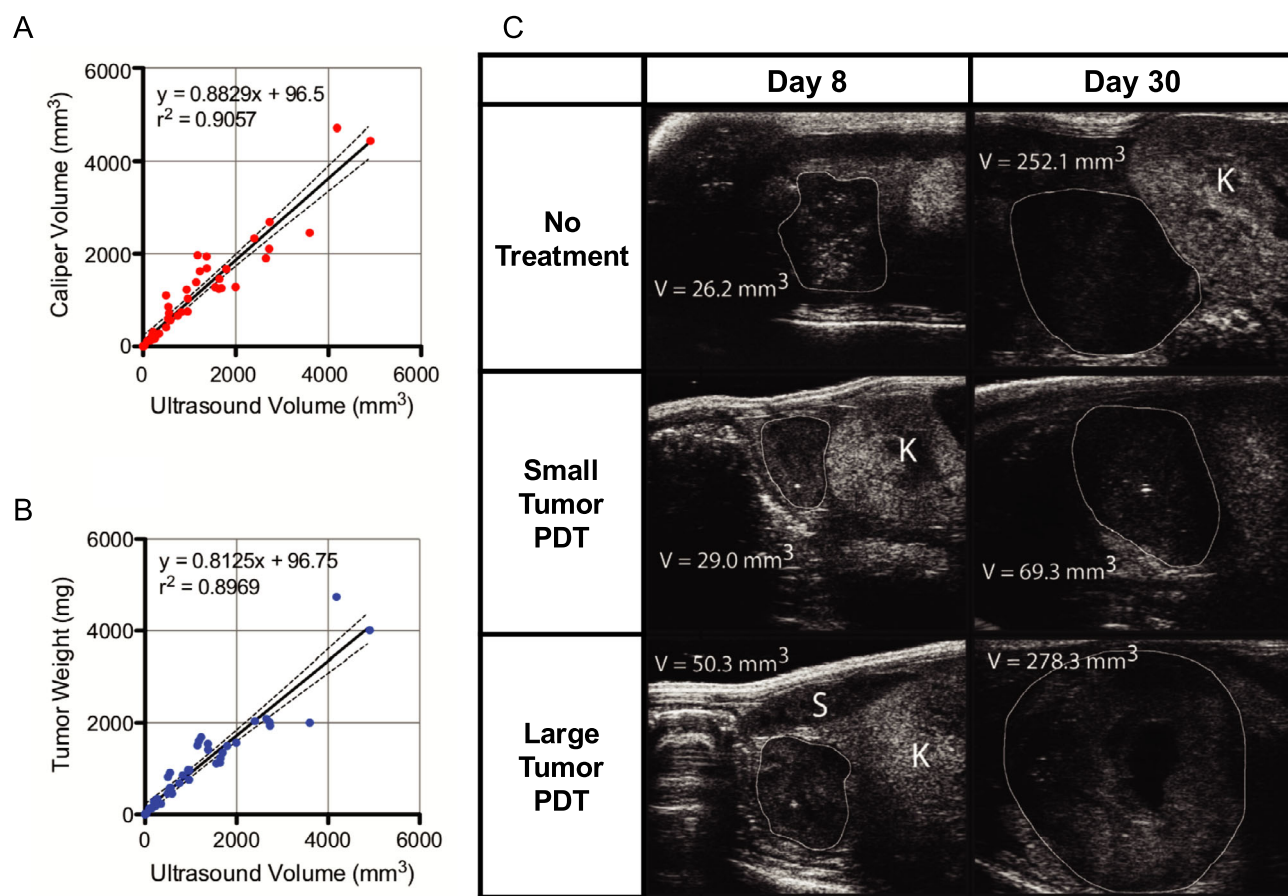
Figure 2. Ultrasound (US) imaging of tumor volume in vivo and correlation with ex vivo tumor weight and volume measured with calipers. (A) Plot of US-calculated tumor volume against caliper-measured volume and (B) weight in milligrams. High predictability of both tumor weight and caliper volume is indicated by the large coefficient of determination, indicative of the effectiveness and accuracy of using US imaging as a means of extracting tumor parameters. (C) Transverse US images of orthotopic pancreatic tumors in mouse, from which orthogonal length measurements were made, and thus volume calculated. Tumor margins and neighboring organs are differentiated based on their respective US echogenicity signatures. White outline = tumor, K = kidney, S = spleen. Adapted with permission from (38).
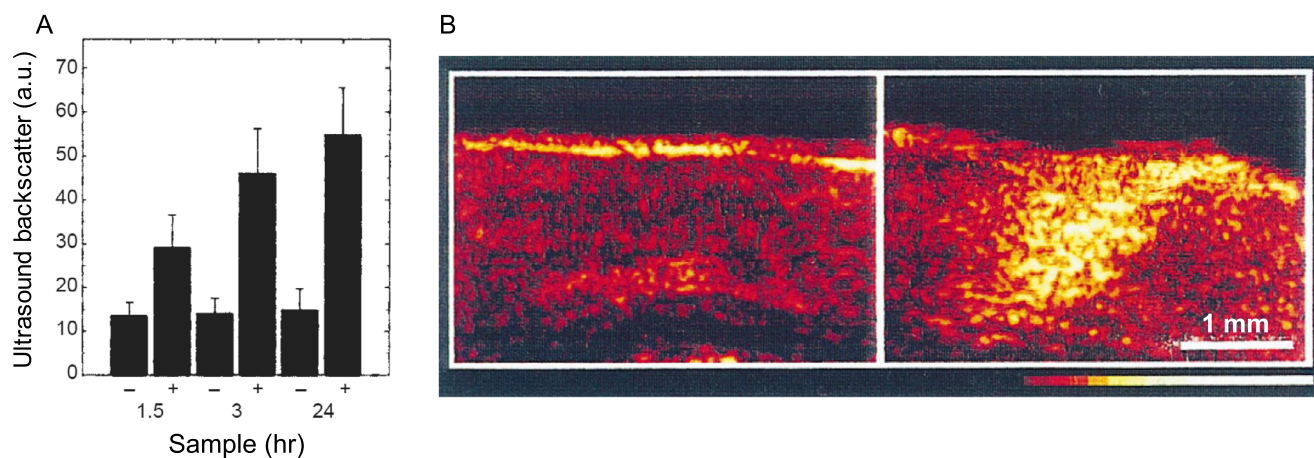

Figure 3. Ultrasound (US) imaging of Photofrin II-PDT in rat brain. (A) Comparison of backscatter variations between various time points from the conclusion of treatment to imaging (40 MHz), each proceeded by a contralateral untreated tissue region serving as a control. Bars labeled "−" correspond to nontreated samples, whereas bars labeled "+" correspond to treated samples. Greatest increase in US backscatter seen 24 h after the conclusion of treatment. Error bars correspond to 1 standard deviation. (B) US imaging of control and treated contralateral regions, respectively. Tissue was imaged immediately following excision 24 h after the administration of Photofrin II-PDT, and US backscatter intensity showed a clear uptick, indicative of a large increase in apoptotic cells in the treated region (and later confirmed histologically). Color bar range: 0 to 256. Adapted with permission from (41).

It should be noted that the tumors in the PDT studies cited here were either subcutaneous or superficial. While US has been extensively used to evaluate the volume of tumors in the breast, pancreas, prostate, etc., and in some cases demonstrating higher accuracy than MRI, there is a dearth of clinical studies where US imaging was the primary modality to monitor PDT response of deep tissue tumors. It is only recently with the advent of various light delivery systems that studies involving PDT of tumors situated deeper within the body are being performed. We anticipate that US imaging will play a major role in monitoring tumor volumes pre- and post-PDT and aid in the positioning of light delivery systems, as will be discussed in a subsequent section.

Monitoring changes in tumor vasculature post-PDT

Blood vessels are a crucial provider of nutrients, signaling highways and avenues for tumoral metastasis (44–49). This makes them a prime target for many therapies including PDT, as their destruction or normalization has been correlated with reductions in tumor volume (50). Imaging therapy-induced changes in blood volume and flow have the potential to be an apt surrogate for treatment efficacy, in lieu of relying on tumor morphology alone. However, microvasculature must also be studied in order to establish a full picture of what is taking place during anticancer treatments, and for this purpose, Doppler ultrasonography has been deployed (51–53). By utilizing the Doppler effect, the frequency shift between the reflected and the initial transmitted US wave is used to determine whether objects are moving toward or away from the transducer, providing data on both the movement direction and speed of the target. This applies to every moving object in the imaging window, be it in the circulatory system or surrounding tissue. Traditional Doppler US retains data on movement speed and direction while power Doppler does away with them in favor of quantifying US signal strength alone, and can measure blood volume via the assignment of colorimetric values to the strength of the detected US signal (54). Using power Doppler US, Yu *et al.* were able to illustrate tumor perfusion variations between various regions of singular RIF tumors in mice undergoing Photofrin-PDT. Differences in PDT-light fluence rate contributed to this variability, as higher light dose created greater levels of hypoxia heterogeneity when compared to lower light dose (75 *vs* 25 mW cm^{-2}) (52). In addition, Yu *et al.* found that hypoxic tumor bases conferred a greater level of survivability to the region, despite a general increase in maturation markers and increased vascularity when compared to the regions of the tumor more proximal to the surface of the epidermis. By using the lower irradiance of 25 mW cm^{-2}, however, the overall response of the tumor to therapy was far more uniform. Their work highlights the utility of monitoring tumor vascularity, particularly to understand the complex interplay between light fluence variability as it encounters a heterogenous tissue and the difficulty in predicting tumor behavior. In the case of Ohlerth *et al.*'s work, vascularity and perfusion 24 h after PDT in cats with invasive squamous cell carcinomas were monitored using power Doppler US, providing evidence of successful treatment monitoring in nonxenograft cancers (51). Power Doppler US images were collected prior to PDT, 5 min, 1 h and 24 h following PDT using either mTHPC (Foscan) or liposomal mTHPC (Fospeg) (Fig. 4), and vascular fractional area (FA) as a metric for how much of the tumor contained vasculature, mean color level (MCL) of the power Doppler US signal as a metric for how many red blood cells are present in the sample region and color-weighted fractional area (CWFA) which is the product of FA and MCL as a unit of vascularity were calculated. Mean FA and CWFA values of the seven imaged tumors were 29.9% and 17.1%, respectively, prior to PDT, and decreased to 7.8% and 3.8, respectively, at 24 h post-PDT. Overall, the study concluded that neither age, weight and concentration of hemoglobin, nor the concentration of red blood cells (RBCs) had any effects on FA and CWFA measurements and illustrated that power Doppler US imaging is a promising tool for assessing PDT outcomes in naturally occurring cancers.

Ultrasound (US)-guided fiber placement for PDT of deep-seated tumors

The optical absorption and scattering properties of tumors determine the light penetration depth with these tissues. Typically, light delivery to deep-seated tumors has to be done with optical fibers via intratumor light delivery (termed interstitial PDT) (55). Tumors have heterogenous vascular content, and recently Pogue *et al.* have demonstrated that the blood content in tumors attenuates light and can affect PDT efficacy more significantly than drug distribution (56). Hence, the fiber placement in deeply seated tumors has to be carefully designed based on tumor shape, size, blood content, oxygenation and PS distribution. In order to precisely deliver light to deep-seated (several centimeters) lesions, the use of fiber optic needles steered via US imaging has been applied in the clinic. Needles fitted with these fibers provide high contrast in US images (Fig. 5), thereby the user can position them at the desired location while steering clear of critical structures such as arteries, in order to deliver light to the target areas. Harris *et al.* utilized real-time US-guided optical fiber placement in mice and rabbit tumor models where a 0.5-mm optical fiber with a cylindrical diffuser end was fitted through a 21-gauge endobronchial US needle to deliver therapeutic light (57). Furthermore, they also demonstrated that US imaging is useful in providing anatomical information to simulate light propagation in the tumors to enable real-time planning and dosimetry of PDT. In another study, Jerjes *et al.* have reported the successful application of the US-guided fiber placement in the clinic using PS mTHPC (Foscan) on a wide array of maladies ranging from carcinomas, sarcomas, and hamartomas of the head, neck, and upper limbs (58). Most excitingly, they have also demonstrated its efficacy in the palliation of symptoms for several patients with stage IV carcinomas of the tongue, two-thirds of which had been offered no further therapies (Fig. 5) (59). The majority of these patients reported improvements in speech, swallowing and breathing, and many showed tumor growth abatement at the 36-month mark following PDT. More recently, DeWitt *et al.* utilized endoscopic US (EUS)-guided PDT to treat locally advanced pancreatic cancer patients. Specifically, EUS was used to guide the insertion of a 1-cm light diffuser inside the pancreatic tumor. Six out of twelve patients showed increased tumor necrosis post-PDT (60). As PDT continues to proliferate in clinical application (2), fiber optics and US guidance will undoubtedly play a major role in improving its therapeutic effectiveness. An exciting advancement for the treatment of deep lesions has been developed by Bansal *et al.*, as they have crafted implantable sources of PDT-generating light that can be remotely activated in order to treat deep-seated lesions (61). Once placed within the body, these devices can be
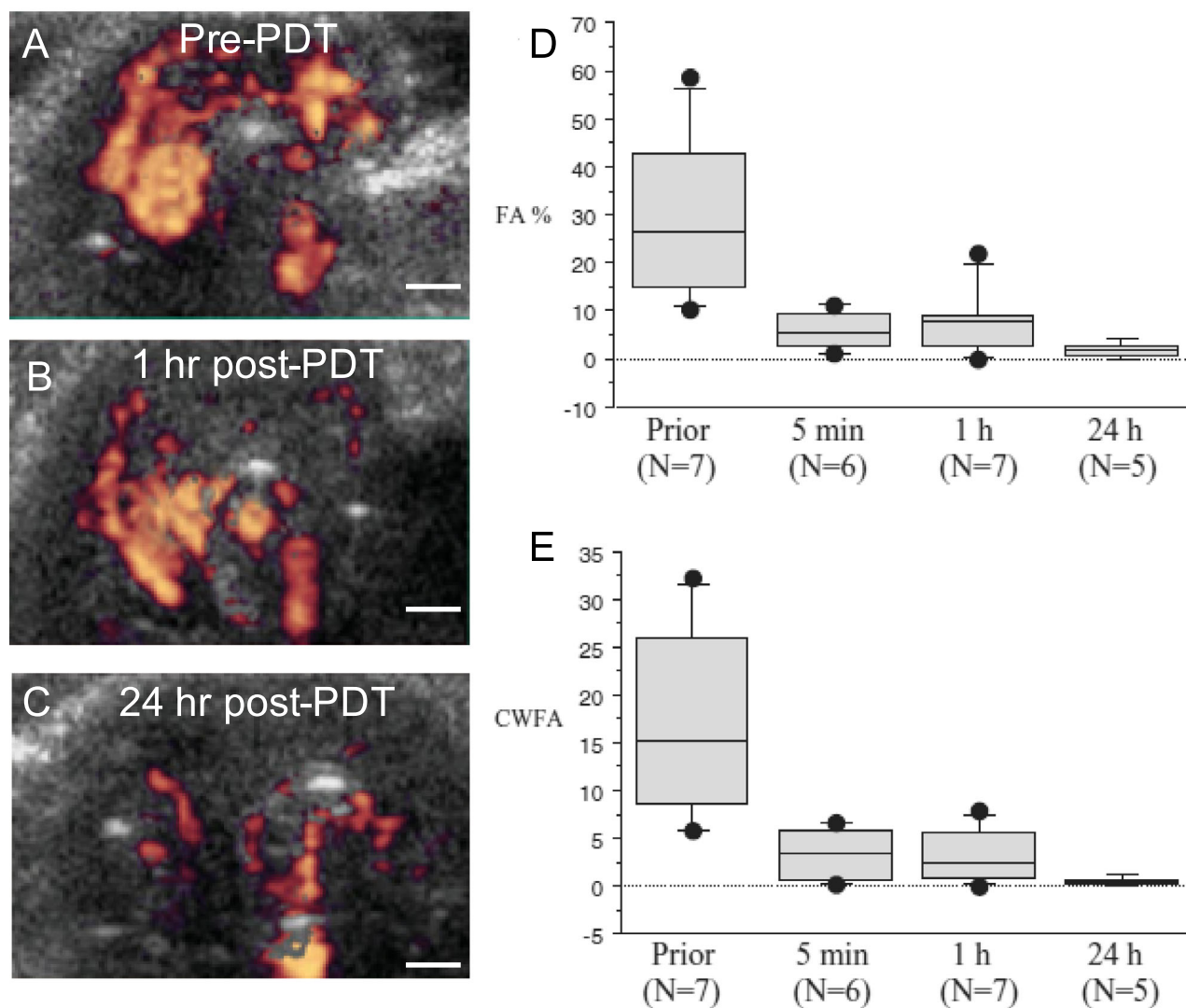
Figure 4. Verification of PDT efficacy using power Doppler US imaging. (A–C) Feline cutaneous squamous cell carcinoma imaged prior to Fospeg/Foscan-PDT, 1 and 24 h post-PDT at 652 nm. (D–E) Vascularity (FA) and blood volume (CWFA) calculated computationally from pixel analysis of power Doppler US signatures of five tumors. Scale bar = 1 cm. A reduction in FA from 29.9% to 7.8% and in CWFA from 17.1% to 3.8% occurred from therapy onset to 24 h afterward. Slight increase in vascularity at the 1-h post-PDT mark was thought to be attributable to partial blood vessel relaxation prior to full closure. Adapted with permission from (51).

activated a multitude of times, necessitating fewer surgeries when compared to the above-mentioned fiber optic needle approach. Bansal *et al*. reported the successful attenuation of tumor growth in mice and state that their system can be used to treat tumors at a depth greater than 3 cm. In addition, these devices can be placed in 3D spatial arrangements around the tumor tissue, which could enable greater control of spatially specific light delivery and fluence adjustments to modify PDT treatments of regions of tumor response variability.

ROLE OF PHOTOACOUSTIC IMAGING IN PDT

Photoacoustic monitoring of PS uptake in the tumor

A dye molecule when excited by a specific wavelength of light releases energy in a radiative (e.g. fluorescence) or nonradiative

(e.g. heat) manner. Generally, the excited electrons in the PS molecules relax to a long-lived triplet state, which then reacts with the substrate environment to generate reactive molecular species for photodynamic therapeutic action. Some PSs also exhibit strong fluorescence, wherein the electron in the excited state can relax back to its ground state by emitting a long-wavelength photon. In the case of nonradiative relaxation of the excited electron, heat production and in some cases the subsequent generation of PA waves can occur when irradiated with nanosecond-pulsed laser light of a proper wavelength (62). Therefore, a PS with low fluorescence quantum yield can generally be expected to act as a good PA contrast agent (63). This is clearly demonstrated by Ho *et al.*, where five different PS molecules were evaluated for their fluorescence and PA properties (30). Zinc phthalocyanine with ~37.5% less fluorescence quantum yield showed a 50% higher PA quantum yield than other commonly used PSs such as protoporphyrin IX (30).
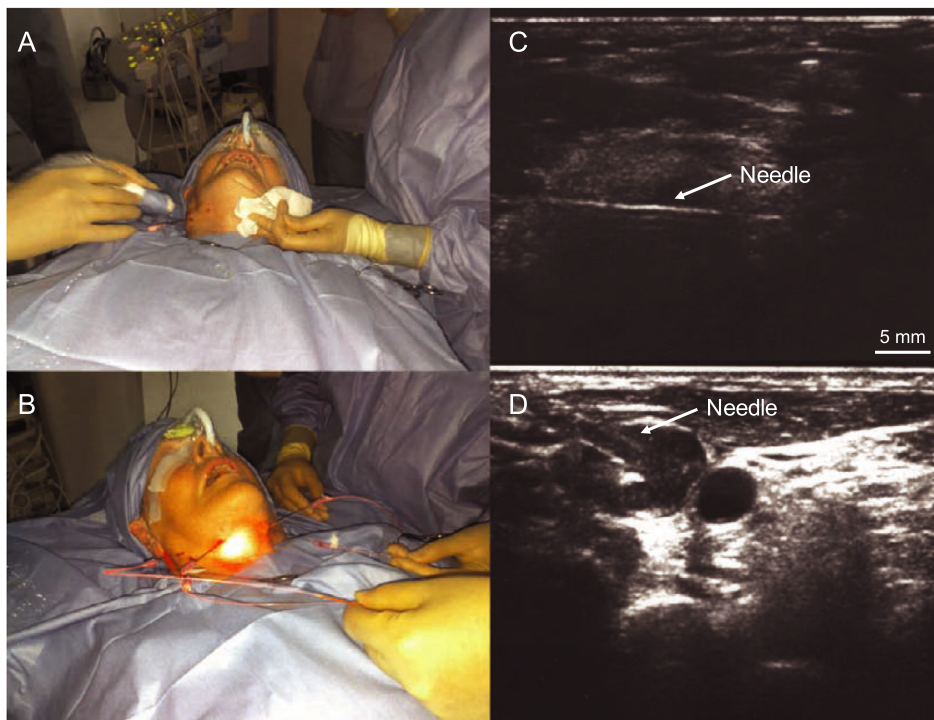
Figure 5. US-guided mTHPC (Foscan)-mediated interstitial PDT of tongue cancer. (A,B) Photographs of the patient undergoing US-guided transcutaneous needle insertion into the tongue base and PDT to the tumor and surrounding lymph nodes. (C) US image showing needle (with light fiber tip) inserted in the tumor mass. (D) US image showing two metastatic cervical lymph nodes (black circles), into one of which the needle is being inserted. Adapted with permission from (59).

Furthermore, the optical absorption coefficient of a PS molecule in "free" form might not be sufficient to obtain a sufficient signal-to-noise ratio (SNR) for PA imaging *in vivo*. As PA signal generation is primarily dependent on the optical absorption properties of the object being imaged, PS molecules encapsulated within nanosystems can provide enhanced PA contrast via the quenching of fluorescence of the PS molecules that are in close proximity to each other (64). For example, Lovell *et al.* showed that PS-conjugated lipids can be used to fabricate nanovesicles called porphysomes that provide high PA contrast and can be used as image-guided theranostic agents (65). When encapsulated in a porphysome, the PA intensity of MB increased by a factor of 5 within the 750–800 nm excitation range. Several studies are ongoing to monitor PA signal change as these nanoliposomal constructs or PS molecules degrade in response to PDT or the tumor microenvironment. Verifying the presence or absence of PS in the lesion is a key deciding factor for the continuation or cessation of further light irradiation for PDT. A more detailed discussion on nanotheranostic agents is provided in a later part of this review.

Photoacoustic monitoring of PDT-induced vascular damage

As previously mentioned, vasculature provides a singular source of a multitude of tumor-related targets. US imaging has been proven to be a powerful tool for assessing changes in blood flow, cellular morphology, and general tumor volume and structure during PDT. PA imaging further adds to the diagnostic arsenal by providing a means to image vascular structural changes, by imaging the endogenous chromophore hemoglobin in blood. The optical absorption properties of hemoglobin are distinct and

higher than normal tissue, which is typically highly optically scattering. This variation of optical absorption properties enables PA imaging to generate maps of vascular structure from deep tissues. The work by Rohrbach *et al* and Xiang *et al.* beautifully illustrates the utility of monitoring vascular destruction due to PDT (66,67). Rohrbach *et al.* utilized PA imaging to show that total vascular area was reduced by 90% following 10 min of PDT and average blood vessel diameter was reduced by 63% (Fig. 6A–C). Similarly, Xiang *et al.* demonstrated that PA imaging can aid in real-time determination of vascular size, structure and dose-dependent damage in mice with basal cell carcinoma following 2-(1-hexyloxyethyl)-2-devinyl pyropheophorbide-a (HPPH)-based PDT. Specifically, a 20% drop in blood vessel size at the 5-min post-PDT mark and a 60% size reduction by 20 min post-PDT (4 mJ cm^{-2} light dose) in a 140-μm blood vessel were observed. Several other optical imaging technologies such as laser Doppler imaging, laser speckle imaging, intravital microscopy and optical frequency domain imaging have been utilized to monitor vascular damage post-PDT (68). Though resolution is sacrificed to obtain vascular information at deeper depths in PA imaging, the previously mentioned optical imaging modalities cannot simultaneously obtain vascular structure, vascular function and PS accumulation profiles in the tumor at deeper depths. Furthermore, the nanosecond-pulsed laser utilized for PA imaging can also be used for PDT activation such as that demonstrated by Xiang *et al*, where vascular PDT with PS protoporphyrin IX (PpIX) was performed with a 532-nm nanosecond-pulsed laser (67). Overall, these studies point to the utility and potential of PA imaging to optimize PDT by providing real-time feedback on dose-dependent vascular changes at deeper depths within tumors.

Photoacoustic monitoring of PDT-induced oxygen saturation change and predicting therapeutic efficacy

Hemoglobin in its oxygenated or deoxygenated state has distinguishable optical absorption properties, that is distinct spectra. Based on these differences, PA signals obtained at multiple wavelengths can be unmixed to quantify blood oxygen saturation and to understand the contribution of oxygenated and deoxygenated hemoglobin in a particular image voxel (69). Studies probing StO_2 with other optical spectroscopic imaging techniques demonstrated that tumors with low StO_2 or hypoxic pretreatment values did not respond to PDT (70). While these studies have provided insights into PDT's mechanism of action and impact on tumor vascular function, PA imaging has a major advantage over other spectroscopic methods as it allows noninvasive, longitudinal and highly spatially resolved monitoring of StO_2 content of the whole tumor volume. Shao *et al.* demonstrated the capabilities of PA imaging to monitor real-time changes in oxygen levels post-PDT while simultaneously measuring alterations in the blood vessel size (71). In their study, a 40% drop in StO_2 levels ~18 min post-PDT followed by a recovery to 20% less than pretreatment values was observed, while constriction of the blood vessels was observed 30 min after PDT (Fig. 6D). Treatment-induced time-dependent mechanisms of vascular shutdown are poorly understood phenomena. Monitoring of vessel size with PA imaging post-treatment, such as that demonstrated by Shao *et al.* (71) and Xiang *et al.* (67), showcases examples of the need for imaging modalities such as PA for providing deeper insights into therapeutic mechanisms of action. In another study, Neuschmelting *et al.* performed vasculature-targeted PDT with PS WST11 (activated at 753 nm and cleared from the mouse body in 20 mins) and monitored StO_2 levels within the tumor vasculature (72). The success of the PDT regimen's goal of vascular destruction was verified from a 60% reduction in StO_2 content one hour following PDT (Fig. 7). Furthermore, they also showed that PA-pulsed illumination alone, at a wavelength of 753 nm, was sufficient to activate PS WST11. This enabled PA imaging of PS uptake, the initiation of PDT and the monitoring of the therapeutic end point of vascular shutdown, all with the same system.

PA imaging's ability to generate 3D maps of tumor oxygenation status opens up new avenues for predicting PDT treatment efficacy. Given the heterogenous microenvironment of tumors, PA imaging can be utilized to map regions within the 3D tumor volume that were responsive or nonresponsive to a treatment (73). This is not possible with other spectroscopic optical imaging techniques that can measure oxygen saturation (74). Using benzoporphyrin derivative (BPD) as their PS, Mallidi *et al.* analyzed 3D PA images of oxygen saturation and built statistical algorithms to predict recurrence of glioblastomas post-PDT (Fig. 8). To begin with, the authors studied the oxygen saturation changes in mice at various time points post-PDT. The study showed an 85% decrease in StO_2 values in responsive tumors 24 h following PDT, while nonresponsive tumors did not show a significant change in StO_2 values at 6 h or 24 h post-PDT. Another important factor that can affect PDT response is the proper interval between PS administration and the initiation of PS excitation, termed the drug–light interval (DLI). Mallidi *et al.*'s study corroborates previous findings in the field that BPD-based PDT is most effective when the PS is localized to the vasculature (shorter DLI) than within the tumor cells themselves (longer DLI). Utilizing 3D StO_2 maps at 24 h post-PDT available via PA imaging, Mallidi *et al.* built a prediction model that could precisely gauge areas of nonresponsiveness within a given tumor. Recurrence that could visually be monitored only several weeks post-PDT can now be evaluated via PA imaging within 24 h post-PDT. This methodology provides a powerful tool that can be utilized in designing subsequent PDT doses or in designing combination treatments with other anti-angiogenic therapies (73) (Fig. 8).

Photoacoustic measurement of oxygen content in tumors

The presence of oxygen in the vicinity of an excited PS molecule is key for the generation of reactive oxygen species. However, photochemical depletion of local oxygen content is generally not accounted for in the same fashion as is the presence of PS in the lesion due to limited availability of imaging techniques that can measure partial pressure of oxygen pO_2 values. Several studies monitored PDT's impact on dynamic changes in tissue oxygenation (pO_2 levels) with invasive single
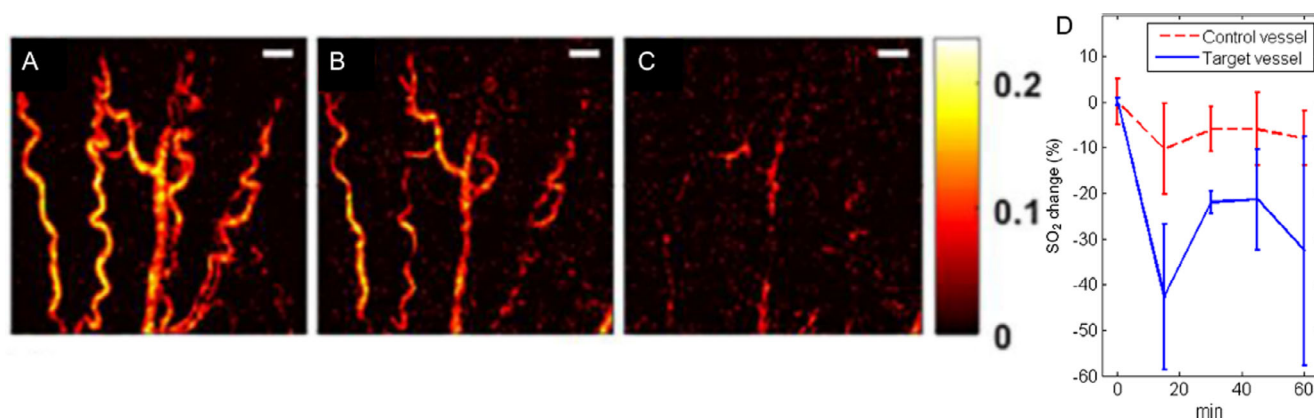
Figure 6. Monitoring changes in vasculature due to PDT using PA imaging. Validation of pre- and post-HPPH-PDT changes in vasculature of basal cell carcinoma-harboring mice with PA imaging, taken before PDT administration (A), 1 min post-PDT (B) and 10 min post-PDT (C). Vascular area was reduced by 49% and 90%, and blood vessel diameter was reduced 23% and 63%, respectively. Scale bar = 500 μm. (D) Example of StO_2 decrease and return to near-endogenous levels during verteporfin-based PDT in the mouse ear blood vessel. Adapted with permission from (66) and (71).

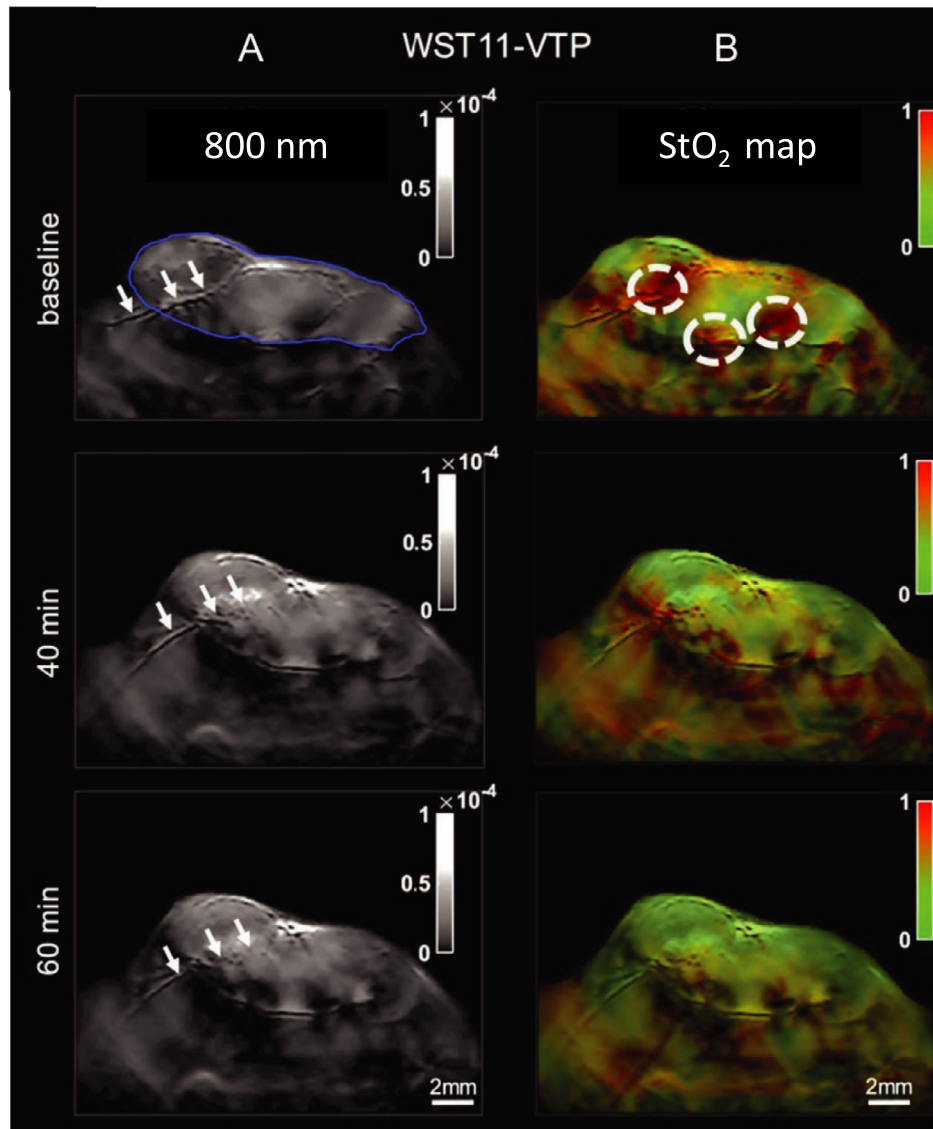**Figure 7.** Photoacoustic imaging (multispectral optoacoustic imaging) of StO_2 levels in renal carcinoma tumors following WST-11-mediated PDT. (A) Imaging of vascular morphological changes at baseline, 40 and 60 min post-PDT. Blue outline of top-left panel indicates tumor boundary, and white arrows point to a major vessel traversing through the tumor. At 60 min post-PDT, clear structural ablation of this vessel can be seen. (B) StO_2 map of treated region, indicating time-dependent drop in StO_2 content (shift from red (high) to green (low) StO_2 values). Adapted with permission from (72).

micro-electrodes, such as the Eppendorf probes. For example, Pogue *et al.* demonstrated that pO_2 changes were heterogenous and that the lower pO_2 regions responded differently than the higher pO_2 regions, potentially as a factor of lesser blood flow rates (75). The Eppendorf probe-based methods to measure pO_2 have significant limitations, including their inability to produce 2D tissue pO_2 maps, preventing them from being widely used in PDT research. Recently, Shao *et al.* have reported a direct and noninvasive PA lifetime imaging method that can produce 2D maps of tissue pO_2 (Fig. 9). Here, the excited triplet state of oxygen-sensitive dye methylene blue (MB) was used to assess the oxygen content within cells (76). By "pumping" the MB molecule with a 650-nm laser and causing it to shift into its excited triplet state, then "probing" (matching) its emission wavelength with an 810-nm laser, the resulting PA signal may be teased out with an US transducer. This technique, called photoacoustic

lifetime imaging (PALI), could become a powerful tool for the rapid assessment of PDT with high spatial resolution of cellular oxygen content. Data on the localization of oxygen in tumors as a factor of pH and temperature alterations from therapy or inflammatory responses would be extremely useful for understanding the more nuanced behaviors of cells as they undergo PDT.

THERANOSTIC NANOMATERIALS FOR IMAGE-GUIDED PDT

The effectiveness of a PDT regimen depends on PS deliverability to the tumor, confirming the intratumoral or intracellular localization of the PS delivery, and utilizing the proper wavelength and light fluence to initiate PDT. A major concern for the older generation of PSs had been off-site cutaneous photosensitivity which
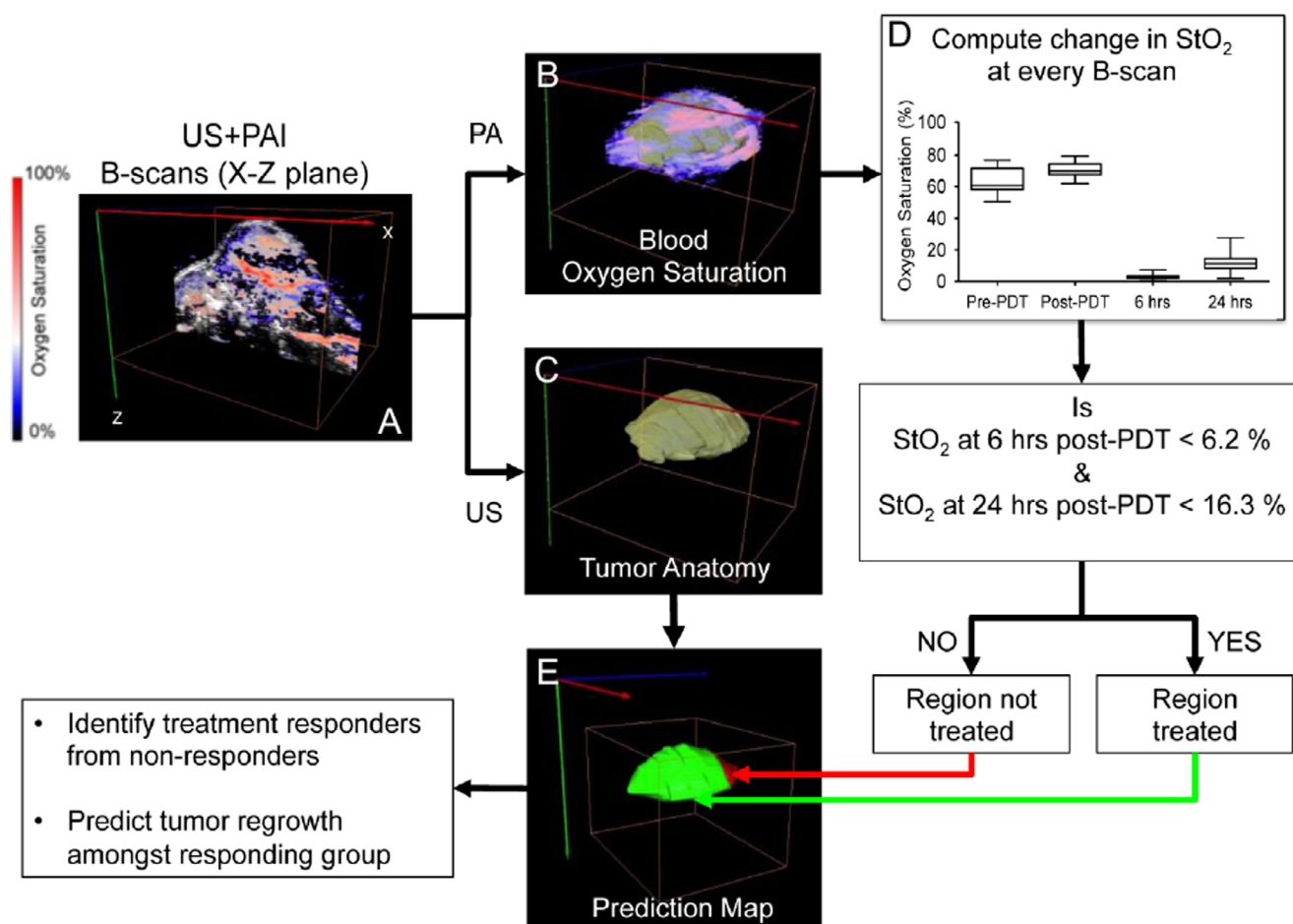
Figure 8. Schematic representation of the image processing workflow of predicting PDT treatment response from 3D ultrasound (US) and PA images. (A) Example slice of combined PA and US image of tumor anatomy and StO$_2$ content, respectively. (B) 3D StO$_2$ overlaid on tumor anatomy map, and (C) US-imaged tumor anatomy alone. Each StO$_2$ value of a given region in a slice (A) is then fed into D: the computational pipeline for determining StO$_2$ variability and thus treatment responsiveness. Should the StO$_2$ values satisfy the requirements of both the 6-h and 24-h post-PDT cutoffs, a Boolean value corresponding to red (not responsive to treatment) or green (responsive to treatment) is then used to reconstruct a 3D map of regional tumor responsiveness (E). Adapted with permission from (73).

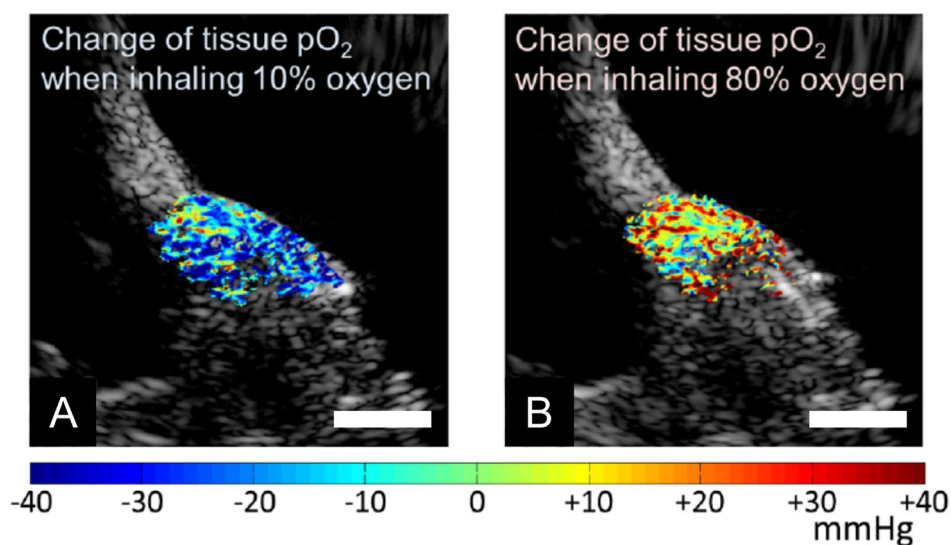**Figure 9.** Demonstration of photoacoustic lifetime oxygen monitoring in vivo. Ultrasound images (grayscale) overlaid with pseudocolored PALI images of various oxygen concentrations. Both the left and right images are from the mouse hind limb. The localized partial pressures of oxygen of a resting mouse inhaling either 10% (A) or 80% (B) oxygen, respectively. Scale bar = 5 mm. Adapted with permission from (76).

decreased the enthusiasm for this modality (77). The recent burgeoning of the nanotechnology field has enabled the encapsulation or absorption of PS molecules into nanoconstructs which can target tumors passively, through leaky vasculature and enhanced permeability and retention (78), or actively via various mechanisms as reviewed elsewhere (79,80). The nanotechnology-based specific delivery of the PS has dramatically decreased off-site toxicity, and their combination with imaging modalities that can monitor the distribution and activity of these nanoconstructs has renewed interest in image-guided PDT (77,81–84). All manner of therapeutic agents, from tumor-specific antigens on the outer surface to ribonucleic acids contained within a nanoparticle, can be combined and tuned to specific signatures such as pH, cell surface markers, or the transcriptional profiles of the target tumor. In addition, contrast agents may be placed on the periphery or within the core of a nanoparticle, as can various sources of ROS generation. Overall, the therapeutic nanotoolbox has greatly increased in size and scope, to include the delivery of multiple PSs and/or other therapeutics. From these advances, understanding each one of them in the context of biocompatibility, tumoral destruction and synergistic or discordant effects is essential for their proper deployment. Specifically, in this section we will review the nanoparticles that can provide either US or PA contrast enhancement and/or ROS generation while simultaneously delivering PSs to the tumor with increased precision.

Gas-filled microbubbles are excellent US contrast agents as gaseous media has greater acoustic impedance than that of fluids and biological tissues. Due to their size, they are purely intravascular tracers and do not extravasate into the tumor interstitium. The US signal intensity is dependent on the microbubble (either passively or specifically targeted to a cancer biomarker) concentration at the target site. Continuous imaging of microbubbles in the tumor vasculature can be quantified, color coded and displayed on top of structural US images to identify regions of abnormal perfusion (85). Cornleis *et al.* showed that contrast-enhanced US (CEUS) imaging can be used to image PS WST11-based PDT-induced vascular damage (86). Though survival and treatment efficacy were not assessed in this study, CEUS images showed good correlation with histology images of necrosis. Microbubbles can also act as PS delivery agents, wherein PSs can be encapsulated in the core, absorbed onto the surface or incorporated into the lipid layers of the microbubble as demonstrated by Huynh *et al.* (87). Furthermore, the outer shell of the microbubble can be coated with proteins, lipids and polymers for enhanced tumor targeting (88). Unfortunately, microbubble deployments have been limited by low stability, short half-lives and a lack of prolonged circulation time, all of which complicate the assessment of successful PS delivery. The work of Park *et al.* has sought to address these shortcomings by developing a pH-dependent microbubble that releases CO_2 at tumor-specific pH, which greatly enhanced US signal for the guidance of subsequent PDT via the PS chlorin e6 payload contained within (89). Similarly, You *et al.* developed a novel porphyrin-grafted lipid microbubble in which the specificity of the PS payload was assisted by US-targeted destruction of the microbubbles, adding further spatial control and improving its therapeutic efficacy (88). Another exciting development in the realm of enhanced US-guided PDT came from the research of Sun *et al.*, in which they combined US-targeted PDT with gene therapy to treat triple-negative breast cancer. They achieved this goal by using cationic porphyrin lipid microbubbles loaded with HIF1alpha-siRNA, providing a therapeutic with both enhanced contrast and the added element of interfering with tumor function on the level of the transcriptome (90). The complexities of gene expression provide a multitude of therapeutic targets, from transcription factors (TF) (91) and miRNA-mediated transcriptional up- or downregulation (92), to cis- and transchromosomal long noncoding RNA (lncRNA) bridges, (93–95), all of which contribute to the proteomic profiles and organellar architecture of a cell (96). In the case of Sun *et al.*'s approach, targeting the transcripts of what would then be translated into the HIF1alpha TF provided a means of attacking the source of several downstream products of unbridled cellular activity, as HIF1alpha's transcriptional influence has been correlated with the increase of tumoral glycolysis and vascular endothelial growth factor (VEGF) translation, both of which are hallmarks of tumor proliferation (97) and important factors of PDT's mechanism of action on tumors (5).

Another arena of nanoparticle-based PDT agents are organic and inorganic nanomaterials, alone or in combination with PSs, which can generate ROS (98). As an added bonus, metallic plasmonic nanoparticles are known to exhibit several fold higher absorption spectra than endogenous tissue chromophores, making them conducive to PA monitoring of their uptake in tumors. For example, Lin *et al.* reported the development of a high-PS capacity gold nanoparticle housing PS Ce6 (GV-Ce6), which allows for 3 modes of imaging (near-infrared fluorescence, thermal and PA imaging) in addition to improved tumoral uptake of the PS payload from heat-induced release of the Ce6 cargo (99). Photothermal and photodynamic activation of their gold vesicle-Ce6 NP takes place at the same wavelength of 671 nm, as does the three modes of imaging. Lin *et al.* verified the tumor killing ability of their NP while also illustrating the spatially specific heating caused by 731 nm illumination in the tumors. Pronounced decrease in tumor volume was observed from activation of the GV-Ce6 NP in addition to tumoral pyknosis. In another study, Lin *et al.* reported the synthesis of two-dimensional tellurium nanosheets which are capable of producing ROS and show high PA imaging performance due to their strong near-infrared absorbance, which confers greater activation and imaging depth (100). In addition, Lin *et al.* suggest that their system can be engineered as a nanoplatform for simultaneous PA imaging and PDT. In another study, Ding *et al.* described the preparation of nanocrystallites composed of the water-insoluble PS zinc(II)-phthalocyanine in the form of nanodots, created by applying a cryodesiccation-driven crystallization approach (101). Modification of the surface of the nanodots with Pluronic F127 and folic acid endowed them with excellent water solubility and stealth properties in blood, which lengthens their circulation time by avoiding immunological detection and destruction. Under NIR excitation at 808 nm, the nanodots are shown to produce singlet oxygen and are of low cytotoxicity. Hou *et al.* reported the synthesis of Cu-Sb-S NPs paired with poly(vinylpyrrolidone) (PVP), which exhibited higher photothermal efficiency and thus PDT effectiveness in addition to improved contrast over prior copper-based NPs (102). Sun *et al.* synthesized a perylene diimide zwitterionic polymer PDS-PDI via atom transfer radical polymerization (ATRP), which is capable of inducing both PDT and photothermal therapy (PTT) (103). Finally, Kim *et al.* reported the production of a pluronic nanogel-based carrier for PSs chlorin e6 and gold nanorods, functionalized with chitosan, for a reversal of previously reported PTT-PDT dual therapy sequence

(104). Controlling the quenching of a PS during dual-phototherapeutics involving gold nanorod-mediated PTT had been elusive prior to their novel nanogel design, generally allowing only for the deployment of PDT after PTT. Kim *et al.*'s nanogel allowed for the spatial separation of the gold nanorods and chlorin e6 PS, and thus no PTT-mediated quenching of chlorin e6 took place. As such, Kim *et al.* were able to deploy PDT prior to PTT, resulting in marked tumor size regression in SCC7 tumor-bearing mice, followed by tumor elimination without return at 10 days post-therapy onward. The field of gel-based PDT and PTT agents is an especially exciting one, as future applications may provide greater insight into sensitizer-tumor localization (imaged with US and PA techniques) following treatment courtesy of novel isotropic sample expansion techniques (105). Further examples of theranostic nanoparticles for PDT are listed in Table 1 and are illustrative of the diversity of these techniques and their efficacious potential in treating a wide range of cancers.

Enhancing oxygen content in the microenvironment via nanoagents

Another development in the field of cancer therapeutics for enhancing PDT efficacy is the artificial presentation of exogenous oxygen to tumors. This may seem counterintuitive to the desired therapeutic endpoint of tumor destruction, as greater oxygen availability may lend itself to greater ROS generation by the tumor and thus an increase in cell division cycles and tumor progression. Conversely, shortage of oxygen may send the tumor down a path to hypoxia thus treatment resistance and enhanced metastases (97). The balance between these two avenues is indeed complex (106); however, many studies have shown that the availability of additional oxygen enhances PDT efficacy and thereby greater tumor destruction and better therapeutic endpoint. The PDT process consumes oxygen in a given tissue, the replenishment of which is dependent on local vascular perfusion. If vasculature is destroyed during PDT and the tumor is insufficiently affected, then both the availability of future molecular O_2 for PDT-mediated ROS generation and tumor hypoxia may result. By supplying additional oxygen to the area undergoing PDT, the conversion of molecular O_2 to ROS may be enhanced, and the therapeutic breadth of PDT increased. Gao *et al.* reported a nanoparticle (IHM) containing indocyanine green and hyaluronic acid (HA) in its membrane, which conferred specific targeting to tumors that overexpress the HA receptor CD44 on their surface (107). Within the core of IHM is housed magnesium oxide, which generates O_2 when it encounters H_2O_2 (hydrogen peroxide) (Fig. 10), the levels of which are aberrantly high in cancer cells (108). The resulting available O_2 for conversion to ROS was increased two-fold using Gao *et al.*'s nanoparticle, and ICG provided contrast for PA imaging. One shortfall to the IHM nanoparticle is that Gao *et al.* found it localizing to liver tissues, which was expected as it expressed a HA receptor, but is an important consideration for assessing the localization of PSs to nontarget tissues. Gao *et al.* proposed that this may be addressed by the addition of polyethylene glycol (PEG) to their nanoparticle to confer a more immunologically inert surface. Luo *et al.* developed a similar approach, but instead utilized hemoglobin-ICG in a PLGA core with a lecithin/DSPE-PEG outer membrane, dubbed I-ARCs (109). In this modality, hemoglobin is converted to ferryl-Hb after photodynamic illumination, providing a highly toxic and spatiotemporally specific agent for tumor destruction.

Luo *et al.* reported complete remission of MCF-7 tumors and no recurrence at 30 days post-treatment. The balance of redox dynamics between normal and cancerous tissues is a complicated affair, and great care must be taken to understand the setting in which these treatments are applied in order to avoid fueling tumor hypoxia, growth or metastasis. Avoiding immunological degradation is a major hurdle for NP-based therapies, and although PEGylation can make a nanoparticle more immunologically "stealthy," cases of anti-PEG immune responses have been reported in mammals (110). To avoid this, the exciting domain of red blood cell membrane-derived nanoparticles (RBCM-NPs) was developed. By creating these NP formulations with blood extracted from patients, several native cell surface receptors of RBCs are already present on these NPS and can aid in avoiding patient-specific immunological responses. This corresponds to greatly improved circulation times, which can reach up to 120 days. Xia *et al.* reported on a number of developments in this arena where patient-specific RBC character can be mapped onto the RBCM-NP theranostic agents (111). Further preclinical testing of such novel theranostic nanoagents for US and PA image-guided PDT is currently underway by several groups. Given the rate at which interdisciplinary collaborations between imaging and nanotechnology research groups is accelerating in both academia and industry, we anticipate the clinical translation of these nanotheranostic agents for PDT applications to come to fruition within the next few decades.

CONCLUSIONS AND FUTURE DIRECTIONS

PDT has tremendous potential for being at the forefront of the therapeutic battle against cancer. However, it is currently restricted to being an adjunct therapy or is employed for palliative care (5) due to hurdles such as the phototoxicities associated with the earlier generation of PSs and the unavailability of accurate dosimetry design strategies. With the advent of novel imaging technologies, nanotechnology-enabled PS drug delivery, clearer understanding of the macroscopic and microscopic mechanisms involved in PDT, and the availability of light fiber delivery systems and dosimetry tools, PDT is well on its way to becoming a primary clinical treatment modality. In this review, we present the essential role that US and PA imaging could play in catapulting PDT to the forefront of cancer therapy. We discussed the utility of these imaging techniques in structurally and functionally characterizing tumors throughout the PDT pipeline, the design and deployment of optical fiber-based modalities, the monitoring of tumor oxygenation status pre-, during, and post-PDT, and finally image-guided enhanced PDT-enabling nanotechnologies.

The low-cost, mobile, high-throughput, real-time acquisition, noninvasive and nonionizing nature of US imaging has made it a key modality to monitor tumor volume. The availability of various clinically approved transducers such as the endoscopic, endocavity, endovaginal, pencil and transesophageal US probes enables the imaging of tumors in the internal structures or organs such as the pancreas, digestive tract and prostate. Only a handful of clinical studies exist that compared the performance of USI and MRI, the other nonionizing imaging modality also used to measure tumor volume and stage cancer. For example, Kim *et al.* showed that endoscopic US (EUS) imaging had a similar sensitivity, specificity and accuracy to MRI (statistically insignificant; *P*-value > 0.05) in pancreatic cysts (112). The study by Fernández-Esparrach *et al.* in 90 patients with rectal cancer concluded that

Table 1. List of theranostic nanomaterials that deliver photosensitizer and also act as US and/or photoacoustic contrast agents.

Nanomaterial	Model	Photosensitizer dose/DLI	Imaging parameters	Tumor targeting	Ref
		Nanoagents for US contrast and delivering PS			
Porphyrin-grafted lipid microbubble (PGL-MB)	PC3 Human prostate cancer xenograft in mice	Porphyrin 650 nm, 200 mW.cm^{-2} 4 h after low-frequency US (LFUS)	US @ 1 MHz to monitor NP accumulation at tumor	Porphyrin-tumor affinity, US-targeted microbubble destruction (UTMD)	(88)
Ce6-loaded CaCO$_3$ core and PEG shell	MCF-7 Human breast cancer *in vitro*	Ce6 671 nm, 6 J.cm^{-2} 0 h DLI	US @ 40 MHz to assess NP's US contrast for 3 h	CaCO3 causing PS release at tumoral pH	(89)
Porphyrin-grafted lipid (CPGL) microbubble loaded with HIF 1α siRNA (siHIF@CpMB)	MDA-MB-231 Human breast cancer injected in mice	Porphyrin 650 nm, 200 mW.cm^{-2} 6 h DLI	US @ 3-12 MHz to monitor MB uptake in tumor	Porphyrin-tumor affinity, UTMD	(90)
		Nanoagents for photoacoustic contrast and delivering PS			
Dox-loaded, folate receptors α (FRα) targeted MTX-decorated self-assembled zinc phthalocyanine–soybean phospholipid complex NPs (DZSM)	4T1 Human breast cancer cells Subcutaneous tumors	ZnPc-SPC (ZS) complex 638 nm, 1000 mW.cm^{-2} 24 h DLI	PA imaging @ 638 nm to monitor DZSM accumulation at tumor site	Folic acid (FA) receptor-mediated tumor uptake	(140)
Hyaluronic acid (HA) coupled with chlorin e6 (Ce6) via adipic dihydrazide (ADH) forming HA-ADH-Ce6 conjugates and self-assembly into HACE NPs.	A549 Human lung cancer Subcutaneous tumors	Ce6 660 nm, 160 mW.cm^{-2} 24 h DLI	PA imaging @ 680 nm to monitor HACE NP accumulation at tumor	HA specificity to CD44 on tumor	(127)
Ce6 bound to HA nanoparticle with perfluorohexane core (PFH@HSC)	MDA-MB-231 Human breast cancer Subcutaneous tumors	Ce6 660 nm, 100 mW.cm^{-2} 4 h DLI	PA imaging @ 690-900 nm to monitor hypoxia relief and PFH@HSC accumulation at tumor	EPR and HA specificity to CD44 on tumor	(128)
Diketopyrrolopyrrole (DPP)–triphenylamine (TPA) NP	HTC-116 Human colorectal cancer cells Subcutaneous tumors	DPP-TPA 660 nm, 1 W·cm^{-2} 2 h DLI	PA imaging @ 680 nm to monitor DPP-TPA NP accumulation at tumor	EPR and PA-guided activation	(129)
Perylene diimide zwitterionic polymer (PDS-PDI)	MDA-MB-231 Human breast cancer injected in mice	Perylene-3,4,9,10-tetracarboxylic diimide (PDS) 660 nm, 500 mW.cm^{-2} 6 h DLI	PA imaging @ 660 nm to monitor PDS-PDI accumulation at tumor	EPR and PA-guided activation	(103)
Tellurium nanosheets functionalized with glutathione (GSH)	HepG2 Human liver cancer injected into mice	Te nanosheets 670 nm, 160 mW.cm^{-2} 0 h DLI	PA imaging @ 680-980 nm to confirm tumor uptake of Te nanosheets + GSH	EPR and PA-guided activation	(100)
Cell membrane-derived shell and a methylene blue and cisplatin (Pt) loaded gelatin nanogel core (MPV)	4T1 Murine breast cancer orthotopic tumors in mice	Methylene blue 671 nm, 450 mW.cm^{-2} 1 h and 4 h DLI	PA imaging @ 680 nm to monitor intratumoral deposition of MPV	EPR and PA-guided activation	(130)
Pc core and four ethanolamine and phthalocyanine-difunctionalized poly (glycidyl methacrylate) arms NP (Pc-PGEA/Pc-3) containing p53	C6 Rat glioma injected in mice	Pc-PGEA/Pc NPs 700 nm, 800 mW.cm^{-2} 0 h DLI	PA imaging @ 680-980 nm to monitor Pc-PGEA/Pc accumulation at tumor	EPR and PA-guided activation	(131)
BODIPY within amphiphilic DSPE-mPEG5000	A549 Human lung cancer subcutaneously injected in mice	BODIPY 730 nm, 200 mW.cm^{-2} 0.5 h DLI	PA imaging @ 760 nm to assess enhanced permeability and retention (EPR) and lysosomal accumulation of BODIPY NP	Direct injection, BODIPY accumulation in acidic lysosomes	(132)
Lecithin/DSPE-PEG-FA outer shell containing PCM core housing DOX and diketopyrrolopyrrole (DPP)-BT dye, functionalized with FA (P(DPP-BT/DOX) NP)	HeLa Human cervical cancer subcutaneously injected into mice	DPP-BT 730 nm, 1000 mW.cm^{-2} 24 h DLI	PA imaging @ 730 nm to monitor P(DPP-BT/DOX) NP accumulation at tumor	FA receptor-mediated tumor uptake	(133)

Table 1. (continued)

Nanomaterial	Model	Photosensitizer dose/DLI	Imaging parameters	Tumor targeting	Ref
Silicon 2,3-naphthalocyanine bi (trihexylsilyloxide) (SiNc)	HT-29 Human colorectal cancer injected into mice	SiNC 770nm, 40 mJ .08 – 1 h DLI	PA imaging @ 680-860 nm to monitor SiNC presence in tumor and assessment of SiNC PA signal strength	EPR	(134)
Porphyrin- or phthalocyanine-bridged silsesquioxane nanoparticles (BSPOR and BSPHT)	MCF-7 Human breast cancer cells *in vitro*	BSPOR/BSPHT 800 nm, 4300 mW.cm^{-2} 24 h DLI	PA imaging @ 700 nm to monitor BSPOR and BSPHT accumulation at tumor	Porphyrin-tumor affinity	(135)
Artificial red blood cell loaded with oxygen (IARC)	MCF-7 Human breast cancer injected into mice	ICG 808 nm, 100 mW.cm^{-2} 0.5 h DLI	Spectroscopic PA imaging to monitor ICG, HbO$_2$ and Hb accumulation at tumor	EPR	(109)
ICG-loaded PEGylated silver nanoparticle core/polyaniline shell (Ag@PANI) nanocomposites (ICG-Ag@PANI)	HeLa Human cervical cancer subcutaneously injected into mice	ICG 808 nm/ 1000 mW.cm^{-2} 24 h DLI	PA imaging @ 808 nm to monitor accumulation of ICG-Ag@PANI at tumor	EPR	(136)
ICG-HA nanoparticle embedded with single-walled carbon nanotubes ICGHANP/SWCNTs (IHANPT)	SSC7 Human oral cancer subcutaneously injected in mice	ICG 808 nm/ 800 mW.cm^{-2} 24 h DLI	PA imaging @ 808 nm to monitor IHANP accumulation at tumor	EPR and IHANPT specificity to CD44 on tumor	(137)
MgO$_2$ NP in ICG and hyaluronic acid (HA) NP	SSC7 Human oral cancer xenografted in mice	ICG 808 nm, 800 mW.cm^{-2} 6 h DLI	PA imaging @ 808 nm to monitor NP accumulation at tumor	HA specificity to CD44 on tumor	(107)
Hyaluronic acid (HA)–cystamine–cholesterol (HSC) self-assembling conjugate incorporating IR780 (HSCI NPs)	MDA-MB-231 Human breast cancer injected in mice	IR780 808 nm, 800 mW.cm^{-2} 0 h DLI	PA imaging @ 680-980 nm to monitor HSCI NP accumulation at tumor	EPR and HA specificity to CD44 on tumor	(138)
Iridium-cyanine nanoparticle (IrCy)	4T1 Murine breast cancer syngeneic xenografts in mice	Iridium dye 808 nm, 50 mW.cm^{-2} 24 h DLI followed by IrCy readministration at 48 h and PDT at 72 h	PA imaging @ 815 nm for detecting cyanine dye to monitor biodistribution and accumulation of IrCy at tumor	EPR and PA-guided activation	(139)
Cu-Sb-S functionalized with poly (vinylpyrrolidone) (PVP-Cu-Sb-S) NP	4T1 Murine breast cancer syngeneic xenografts in mice	PVP-Cu-Sb-S NP 808 nm, 1000 mW.cm^{-2} 0 h DLI	PA imaging @ 808 nm for monitoring tumor uptake of PVP-Cu-Sb-S NPs	EPR and PA-guided activation	(102)
Zinc(II)-phthalocyanine nanodots, PEG-folate/ZnPc nanodots (FA-ZnPcNDs)	CNE-2 Human nasopharyngeal cancer injected into mice	ZnPC 808 nm, 500 mW.cm^{-2} 2 h DLI	PA imaging @ 808 nm to monitor FA-ZnPcND accumulation at tumor	FA receptor-mediated tumor uptake	(101)
Polypyrrole with astaxanthin-conjugated bovine serum albumin polymer (PPy@BSA-Astx)	MBA-MD-231 Human breast cancer *in vitro*	Astaxanthin 808 nm, 300 mW.cm^{-2} 6 h DLI	PA @ 808 nm to monitor PPy@BSA-Astx US signal production	Passive targeting	(141)

there was no statistically significant difference in staging the disease between both MRI and EUS (113). Pinkavova *et al.* monitored the size of locally advanced cervical cancer following neoadjuvant chemotherapy and reported that the diagnostic accuracy for predicting tumor volume was similar to MRI; however, MRI showed higher sensitivity than US imaging in this study (114). In another study on 39 breast cancer patients by Lee *et al.*, no significant difference in volume estimation by US imaging or MRI was observed; however, MRI had marginally higher (18.2%) predictive capability than US imaging in evaluating pathologic complete response in patients post-treatment (115). Furthermore, aspects such as technical accuracy, clinician's belief, and the necessity of pursuing surgical resection also

factors into the wide adaptability of US imaging as discussed in a notable study conducted by Spolverato *et al.* (116). A major drawback of US imaging in accurately determining the size of a lesion is due to the hypothetical sound velocity used to calculate backscattered echo round trip time in image reconstruction. Since the velocities vary between various tissues (about 13%), an over- or underestimation of thickness as well as image aberrations could occur and several studies are currently being pursued to resolve this issue via correction of speed of sound values (117,118). Another major drawback is identification of lesion boundaries leading to interoperator variability. Research on various machine learning, artificial intelligence and 3D reconstruction algorithms that can enhance the detection of tumor
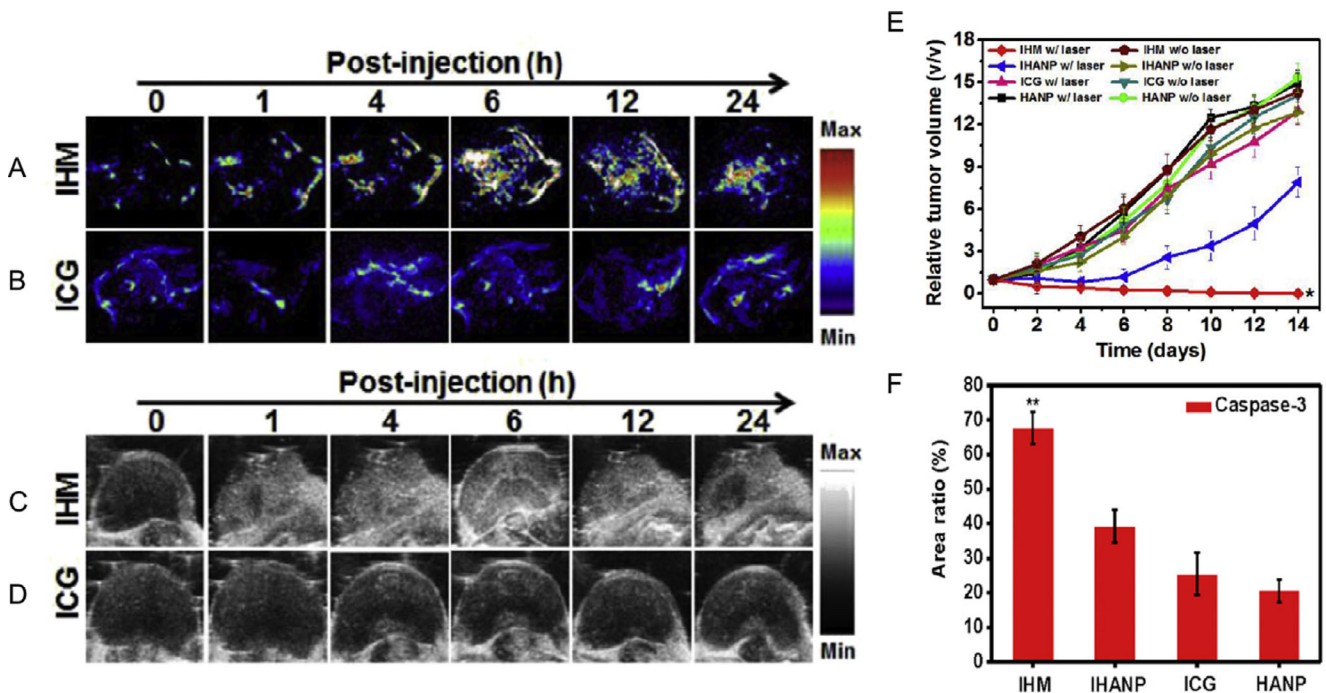
Figure 10. IHM-mediated oxygen delivery for better PDT efficacy. (A and B) PA imaging of IHM and ICG densities in tumors. Maximal accumulation at the 6-h mark. (C and D) Corresponding US image displayed on a gray colormap. Enhanced US signal was observed only in the IHM group and not in the ICG group. (E) Tumor volume reduction is the most effective in the IHM w/laser group when compared to other treatment groups, and (F) corresponding expression of caspase-3, indicative of apoptosis-mediated tumor death following PDT, calculated from histological analysis. Gao *et al.* reported IHM-treated tumors were cured at 14-days, with no recurrence by 30 days. Adapted with permission from (107).

boundaries and reduce operator variability is currently being pursued which will further the utility of USI in PDT treatment monitoring (119).

While US imaging is ubiquitously available for patient care, PA imaging is also making strides in the clinical realm in characterizing prostate, breast and skin cancer lesions (120). As with US imaging, the frequency of the transducer is a major determining factor of resolution in PA imaging. Both in the preclinical and more recently in the clinical realm, PA imaging has gained tremendous popularity due to its capability to measure blood oxygen saturation in 3D at high penetration depth and resolution (69). Though the blood oxygen saturation and partial pressure of oxygen cannot be directly correlated and can generally be described via the Severinghaus equation (121), oxygen saturation maps have shown good correlation with cellular hypoxia markers in several preclinical and clinical studies (69,122). For example, Gerling *et al.* showed good correlation between oxygen saturation and immunohistological hypoxia marker pimonidazole ($R^2 = 0.887$) (123), while a study by Tomaszewski *et al.* showed a moderate correlation ($R^2 = 0.46$) with cellular hypoxia marker carbonic anhydrase (124). In a recent clinical study on breast cancer patients, oxygen saturation levels were not statistically different between the carbonic anhydrase positive and negative cases; however, the total vascular perimeter showed a moderate correlation ($R^2 = 0.43$) with the oxygen saturation level only in the group that had received therapy previously (125). To obtain accurate oxygenation values, robust phantom and *ex vivo* and *in vivo* evaluations and comparisons between partial pressure of oxygen at the cellular level and blood oxygen saturation at the vascular level must be conducted. Moreover, strategies involving light delivery to deeper tissues, PA signal detection and signal processing and unmixing in the presence of additional NIR dyes such as PSs are

being explored to improve accuracy of estimating blood oxygen saturation as recently reviewed by Li *et al.* (69) and Cao *et al.* (122). These research efforts and technological advances in the PA imaging realm are bound to make it a leading technique for designing and monitoring PDT.

Given the recent developments in US and PA imaging technology, including efforts to build low-cost systems (126) and integrated theranostic setups, in the near future we can expect to see a combined US, PA and photodynamic probe that can image the pretreatment tumor condition, adjust PDT dose according to tumor vascular status, oxygenation status and PS concentration in the lesion, and monitor the therapy while PDT action is ongoing. With the advent of better light delivery system, faster data acquisition (by way of high repetition frequency lasers), better image processing algorithms, and transducers with better sensitivity, provides a strong foundation upon which it can be envisioned that the efforts on personalized US imaging and PA-guided PDT treatment strategies will continue advancing the improvement of clinical outcomes in cancer.

REFERENCES

1. Bray, F., J. Ferlay, I. Soerjomataram, R. L. Siegel, L. A. Torre and A. Jemal (2018) Global cancer statistics 2018: GLOBOCAN

estimates of incidence and mortality worldwide for 36 cancers in 185 countries. *CA Cancer J. Clin.* **68**, 394–424.

2. van Straten, D., V. Mashayekhi, H. S. de Bruijn, S. Oliveira and D. J. Robinson (2017) Oncologic photodynamic therapy: Basic principles, current clinical status and future directions. *Cancers (Basel)* **9**, 19.

3. Raab, G. H., A. F. Schneider, W. Eiermann, H. Gottschalk-Deponte, R. Baumgartner and W. Beyer (1990) Response of human endometrium and ovarian carcinoma cell-lines to photodynamic therapy. *Arch. Gynecol. Obstet.* **248**, 13–20.

4. Spring, B. Q., I. Rizvi, N. Xu and T. Hasan (2015) The role of photodynamic therapy in overcoming cancer drug resistance. *Photochem. Photobiol. Sci.* **14**, 1476–1491.

5. Celli, J. P., B. Q. Spring, I. Rizvi, C. L. Evans, K. S. Samkoe, S. Verma, B. W. Pogue and T. Hasan (2010) Imaging and photodynamic therapy: mechanisms, monitoring, and optimization. *Chem. Rev.* **110**, 2795–2838.

6. Celli, J. P., N. Solban, A. Liang, S. P. Pereira and T. Hasan (2011) Verteporfin-based photodynamic therapy overcomes gemcitabine insensitivity in a panel of pancreatic cancer cell lines. *Lasers Surg. Med.* **43**, 565–574.

7. Sun, G., M. A. Anderson, E. C. Gorospe, C. L. Leggett, L. S. Lutzke, L. M. Wong Kee Song, M. Levy and K. K. Wang (2012) Synergistic effects of photodynamic therapy with HPPH and gemcitabine in pancreatic cancer cell lines. *Lasers Surg. Med.* **44**, 755–761.

8. Xie, Q., L. Jia, Y.-H. Liu and C.-G. Wei (2009) Synergetic anticancer effect of combined gemcitabine and photodynamic therapy on pancreatic cancer in vivo. *World J. Gastroenterol.* **15**, 737–741.

9. Peng, Q. and J. M. Nesland (2004) Effects of photodynamic therapy on tumor stroma. *Ultrastruct. Pathol.* **28**, 333–340.

10. Huang, Z., H. Xu, A. D. Meyers, A. I. Musani, L. Wang, R. Tagg, A. B. Barqawi and Y. K. Chen (2008) Photodynamic therapy for treatment of solid tumors–potential and technical challenges. *Technol. Cancer Res. Treat.* **7**, 309–320.

11. Mitsunaga, M., M. Ogawa, N. Kosaka, L. T. Rosenblum, P. L. Choyke and H. Kobayashi (2011) Cancer cell-selective in vivo near infrared photoimmunotherapy targeting specific membrane molecules. *Nat. Med.* **17**, 1685–1691.

12. Li, W., Q. Ma and E. Wu (2012) Perspectives on the role of photodynamic therapy in the treatment of pancreatic cancer. *Int. J. Photoenergy* **2012**, 1–9.

13. Ayaru, L., S. G. Bown and S. P. Pereira (2005) Photodynamic therapy for pancreatic and biliary tract carcinoma. *Int. J. Gastrointest. Cancer* **35**, 1–13.

14. Wolfsen, H. C. (2008) Photodynamic therapy for pancreatic cancer: let's get serious. *Gastrointest. Endosc.* **67**, 961–963.

15. Fan, B.-G. and A. Andrén-Sandberg (2007) Photodynamic therapy for pancreatic cancer. *Pancreas* **34**, 385–389.

16. Pereira, S. (2012) Photodynamic therapy for pancreatic and biliary tract cancer: the United Kingdom experience. *J. Natl. Compr. Canc. Netw.* **10**(Suppl 2), S48–S51.

17. Bown, S. G., A. Z. Rogowska, D. E. Whitelaw, W. R. Lees, L. B. Lovat, P. Ripley, L. Jones, P. Wyld, A. Gillams and A. W. Hatfield (2002) Photodynamic therapy for cancer of the pancreas. *Gut* **50**, 549–557.

18. Huggett, M. T., M. Jermyn, A. Gillams, S. Mosse, E. Kent, S. Bown, T. Hasan, B. Pogue and S. Pereira (2013) Photodynamic therapy of locally advanced pancreatic cancer (VERTPAC study): Final clinical results. *Proc. Spie* **13**, e2–e3.

19. Moesta, K. T., P. Schlag, H. O. Jr Douglass and T. S. Mang (1995) Evaluating the role of photodynamic therapy in the management of pancreatic cancer. *Lasers Surg. Med.* **16**, 84–92.

20. Momma, T., M. Hamblin, H. C. Wu and T. Hasan (1999) Photodynamic therapy of orthotopic prostate cancer with benzoporphyrin derivative: Local control and distant metastasis. *Can. Res.* **58**, 5425–5431.

21. Schreiber, S., S. Gross, A. Brandis, A. Harmelin, V. Rosenbach-Belkin, A. Scherz and Y. Salomon (2002) Local photodynamic therapy (PDT) of rat C6 glioma xenografts with Pd-bacteriopheophorbide leads to decreased metastases and increase of animal cure compared with surgery. *Int. J. Cancer* **99**, 279–285.

22. Kosharskyy, B., N. Solban, S. K. Chang, I. Rizvi, Y. Chang and T. Hasan (2006) A mechanism-based combination therapy reduces local tumor growth and metastasis in an orthotopic model of prostate cancer. *Cancer Res.* **66**, 10953–10958.

23. Wilson, B. C., M. S. Patterson and L. Lilge (1997) Implicit and explicit dosimetry in photodynamic therapy: a New paradigm. *Lasers Med. Sci.* **12**, 182–199.

24. Zhu, T. C. and J. C. Finlay (2008) The role of photodynamic therapy (PDT) physics. *Med. Phys.* **35**, 3127–3136.

25. Pogue, B. W., J. T. Elliott, S. C. Kanick, S. C. Davis, K. S. Samkoe, E. V. Maytin, S. P. Pereira and T. Hasan (2016) Revisiting photodynamic therapy dosimetry: reductionist & surrogate approaches to facilitate clinical success. *Phys. Med. Biol.* **61**, R57–R89.

26. Mallidi, S., S. Anbil, S. Lee, D. Manstein, S. Elrington, G. Kositratna, D. Schoenfeld, B. Pogue, S. J. Davis and T. Hasan (2014) Photosensitizer fluorescence and singlet oxygen luminescence as dosimetric predictors of topical 5-aminolevulinic acid photodynamic therapy nduced clinical erythema. *J. Biomed. Opt.* **19**, 028001.

27. Kamanli, A. F., G. Çetinel and M. Z. Yıldız (2019) A new hand-held singlet oxygen detection system (SODS) and NIR light source based phantom environment for photodynamic therapy applications. *Photodiagn. Photodyn. Ther.* **29**, 101577.

28. Mallidi, S., G. P. Luke and S. Y. Emelianov (2011) Photoacoustic imaging in cancer detection, diagnosis, and treatment guidance. *Trends Biotechnol.* **29**, 213–221.

29. Xu, M. and L. V. Wang (2006) Photoacoustic imaging in biomedicine. *Rev. Sci. Instrum.* **77**, 041101.

30. Ho, C. J. H., G. Balasundaram, W. Driessen, R. McLaren, C. L. Wong, U. S. Dinish, A. B. E. Attia, V. Ntziachristos and M. Olivo (2014) Multifunctional photosensitizer-based contrast agents for photoacoustic imaging. *Sci. Rep.* **4**, 5342–5342.

31. Xia, J., J. Yao and L. Wang (2014) Photoacoustic tomography: principles and advances. *Electromagn Waves (Camb)* **147**, 1–22.

32. Mehrmohammadi, M., S. J. Yoon, D. Yeager and S. Y. Emelianov (2013) Photoacoustic imaging for cancer detection and staging. *Mol. Imag.* **2**, 89–105.

33. Valluru, K., B. Chinni and N. Rao (2011) Photoacoustic imaging: opening new frontiers in medical imaging. *J. Clin. Imaging Sci.* **1**, 24.

34. Ntziachristos, V. and D. Razansky (2010) Molecular imaging by means of multispectral optoacoustic tomography (MSOT). *Chem. Rev.* **110**, 2783–2794.

35. Emelianov, S. Y., P.-C. Li and M. O'Donnell (2009) Photoacoustics for molecular imaging and therapy. *Phys. Today* **62**, 34–39.

36. Mallidi, S., B. Wang, M. Mehrmohammadi, M. Qu, Y.-S. Chen, P. Joshi, S. Kim, K. Homan, A. Karpiouk, R. W. Smalling, K. Sokolov and S. Y. Emelianov. Ultrasound-based imaging of nanoparticles: From molecular and cellular imaging to therapy guidance. In 2009 IEEE International Ultrasonics Symposium, pp. 27–36. IEEE, Proceedings of the 2009 IEEE International Ultrasonics Symposium 2009.

37. Keshava, N. and J. F. Mustard (2002) Spectral unmixing. *IEEE Signal Proc. Mag.* **19**, 44–57.

38. Pigula, M., H.-C. Huang, S. Mallidi, S. Anbil, J. Liu, Z. Mai and T. Hasan (2019) Size-dependent tumor response to photodynamic therapy and irinotecan monotherapies revealed by longitudinal ultrasound monitoring in an orthotopic pancreatic cancer model. *Photochem. Photobiol.* **95**, 378–386.

39. Moore, J. V. and E. Allan (2003) Pulsed ultrasound measurements of depth and regression of basal cell carcinomas after photodynamic therapy: relationship to probability of 1-year local control. *Br. J. Dermatol.* **149**, 1035–1040.

40. Banihashemi, B., R. Vlad, B. Debeljevic, A. Giles, M. C. Kolios and G. J. Czarnota (2008) Ultrasound imaging of apoptosis in tumor response: novel preclinical monitoring of photodynamic therapy effects. *Cancer Res.* **68**, 8590–8596.

41. Czarnota, G. J., M. C. Kolios, J. Abraham, M. Portnoy, F. P. Ottensmeyer, J. W. Hunt and M. D. Sherar (1999) Ultrasound imaging of apoptosis: high-resolution non-invasive monitoring of programmed cell death in vitro, in situ and in vivo. *Br. J. Cancer* **81**, 520–527.

42. Ayers, G. D., E. T. McKinley, P. Zhao, J. M. Fritz, R. E. Metry, B. C. Deal, K. M. Adlerz, R. J. Coffey and H. C. Manning (2010) Volume of preclinical xenograft tumors is more accurately assessed by ultrasound imaging than manual caliper measurements. *J. Ultrasound Med.* **29**, 891–901.

43. Ramasawmy, R., S. P. Johnson, T. A. Roberts, D. J. Stuckey, A. L. David, R. B. Pedley, M. F. Lythgoe, B. Siow and S. Walker-Samuel (2016) Monitoring the growth of an orthotopic tumour xenograft model: multi-modal imaging assessment with Benchtop MRI (1T), high-field MRI (9.4T), ultrasound and bioluminescence. *PLoS ONE* **11**, e0156162.

44. Pasquale, E. B. (2010) Eph receptors and ephrins in cancer: bidirectional signalling and beyond. *Nat. Rev. Cancer* **10**, 165–180.

45. Lockman, P. R., R. K. Mittapalli, K. S. Taskar, V. Rudraraju, B. Gril, K. A. Bohn, C. E. Adkins, A. Roberts, H. R. Thorsheim, J. A. Gaasch, S. Huang, D. Palmieri, P. S. Steeg and Q. R. Smith (2010) Heterogeneous blood-tumor barrier permeability determines drug efficacy in experimental brain metastases of breast cancer. *Clin. Cancer Res.* **16**, 5664–5678.

46. Steeg, P. S. (2006) Tumor metastasis: mechanistic insights and clinical challenges. *Nat. Med.* **12**, 895–904.

47. Buscail, E., A. Chauvet, P. Quincy, O. Degrandi, C. Buscail, I. Lamrissi, I. Moranvillier, C. Caumont, S. Verdon, A. Brisson, M. Marty, L. Chiche, C. Laurent, V. Vendrely, F. Moreau-Gaudry, A. Bedel and S. Dabernat (2019) CD63-GPC1-positive exosomes coupled with CA19-9 offer good diagnostic potential for resectable pancreatic ductal adenocarcinoma. *Translat. Oncol.* **12**, 1395–1403.

48. Das, S. K., D. Sarkar, L. Emdad and P. B. Fisher (2019) MDA-9/Syntenin: An emerging global molecular target regulating cancer invasion and metastasis. *Adv. Cancer Res.* **144**, 137–191.

49. Vaupel, P., F. Kallinowski and P. Okunieff (1989) Blood flow, oxygen and nutrient supply, and metabolic microenvironment of human tumors: A review. *Can. Res.* **49**, 6449.

50. Folkman, J. (1996) Fighting cancer by attacking its blood supply. *Sci. Am.* **275**, 150–154.

51. Ohlerth, S., D. Laluhova, J. Buchholz, M. Roos, H. Walt and B. Kaser-Hotz (2006) Changes in vascularity and blood volume as a result of photodynamic therapy can be assessed with power Doppler ultrasonography. *Lasers Surg. Med.* **38**, 229–234.

52. Yu, G., T. Durduran, C. Zhou, H. W. Wang, M. E. Putt, H. M. Saunders, C. M. Sehgal, E. Glatstein, A. G. Yodh and T. M. Busch (2005) Noninvasive monitoring of murine tumor blood flow during and after photodynamic therapy provides early assessment of therapeutic efficacy. *Clin. Cancer Res.* **11**, 3543–3552.

53. Gee, M. S., H. M. Saunders, J. C. Lee, J. F. Sanzo, W. T. Jenkins, S. M. Evans, G. Trinchieri, C. M. Sehgal, M. D. Feldman and W. M. F. Lee (2001) Doppler ultrasound imaging detects changes in tumor perfusion during antivascular therapy associated with vascular anatomic alterations. *Can. Res.* **61**, 2974.

54. Babcock, D. S., H. Patriquin, M. LaFortune and M. Dauzat (1996) Power Doppler sonography: Basic principles and clinical applications in children. *Pediatr. Radiol.* **26**, 109–115.

55. Shafirstein, G., D. Bellnier, E. Oakley, S. Hamilton, M. Potasek, K. Beeson and E. Parilov (2017) Interstitial photodynamic therapy-a focused review. *Cancers (Basel)* **9**, 12.

56. Jermyn, M., S. C. Davis, H. Dehghani, M. T. Huggett, T. Hasan, S. P. Pereira, S. G. Bown and B. W. Pogue (2014) CT contrast predicts pancreatic cancer treatment response to verteporfin-based photodynamic therapy. *Phys. Med. Biol.* **59**, 1911–1921.

57. Harris, K., E. Oakley, D. Bellnier and G. Shafirstein (2017) Endobronchial ultrasound—guidance for interstitial photodynamic therapy of locally advanced lung cancer—a new interventional concept. *J. Thoracic Dis.* **9**, 2613–2618.

58. Jerjes, W., T. Upile, Z. Hamdoon, F. Nhembe, R. Bhandari, S. Mackay, P. Shah, C. A. Mosse, J. A. Brookes, S. Morley and C. Hopper (2009) Ultrasound-guided photodynamic therapy for deep seated pathologies: prospective study. *Lasers Surg. Med.* **41**, 612–621.

59. Jerjes, W., T. Upile, Z. Hamdoon, S. Abbas, S. Akram, C. A. Mosse, S. Morley and C. Hopper (2011) Photodynamic therapy: The minimally invasive surgical intervention for advanced and/or recurrent tongue base carcinoma. *Lasers Surg. Med.* **43**, 283–292.

60. DeWitt, J. M., K. Sandrasegaran, B. O'Neil, M. G. House, N. J. Zyromski, A. Sehdev, S. M. Perkins, J. Flynn, L. McCranor and S. Shahda (2019) Phase 1 study of EUS-guided photodynamic therapy for locally advanced pancreatic cancer. *Gastrointest. Endosc.* **89**, 390–398.

61. Bansal, A., F. Yang, T. Xi, Y. Zhang and J. S. Ho (2018) In vivo wireless photonic photodynamic therapy. *Proc. Natl Acad. Sci. USA* **115**, 1469–1474.

62. Nie, L. and X. Chen (2014) Structural and functional photoacoustic molecular tomography aided by emerging contrast agents. *Chem. Soc. Rev.* **43**, 7132–7170.

63. Zhang, Y. and J. F. Lovell (2017) Recent applications of phthalocyanines and naphthalocyanines for imaging and therapy. *Wiley Interdisciplinary Rev.* **9**, e1420.

64. Yuan, A., J. Wu, X. Tang, L. Zhao, F. Xu and Y. Hu (2013) Application of near-infrared dyes for tumor imaging, photothermal, and photodynamic therapies. *J. Pharm. Sci.* **102**, 6–28.

65. Lovell, J. F., C. S. Jin, E. Huynh, H. Jin, C. Kim, J. L. Rubinstein, W. C. W. Chan, W. Cao, L. V. Wang and G. Zheng (2011) Porphysome nanovesicles generated by porphyrin bilayers for use as multimodal biophotonic contrast agents. *Nat. Mater.* **10**, 324–332.

66. Rohrbach, D. J., H. Salem, M. Aksahin and U. Sunar (2016) Photodynamic therapy-induced microvascular changes in a nonmelanoma skin cancer model assessed by photoacoustic microscopy and diffuse correlation spectroscopy. *Photonics* **3**, 48.

67. Xiang, L., D. Xing, H. Gu, D. Yang, S. Yang, L. Zeng and W. R. Chen (2007) Real-time optoacoustic monitoring of vascular damage during photodynamic therapy treatment of tumor. *J. Biomed. Opt.* **12**, 014001–014001.

68. Mallidi, S., B. Q. Spring and T. Hasan (2015) Optical imaging, photodynamic therapy and optically triggered combination treatments. *Cancer J.* **21**, 194–205.

69. Li, M., Y. Tang and J. Y. Photoacoustics (2018) Photoacoustic tomography of blood oxygenation: a mini review. *Photoacoustics* **10**, 65–73.

70. Ahn, P. H., J. C. Finlay, S. M. Gallagher-Combo, H. Quon, B. W. Jr O'Malley, G. S. Weinstein, A. Chalian, K. Malloy, T. Sollecito, M. Greenberg, C. B. 2nd Simone, S. McNulty, A. Lin, T. C. Zhu, V. Livolsi, M. Feldman, R. Mick, K. A. Cengel and T. M. Busch (2018) Lesion oxygenation associates with clinical outcomes in premalignant and early stage head and neck tumors treated on a phase 1 trial of photodynamic therapy. *Photodiagnosis Photodyn. Ther.* **21**, 28–35.

71. Shao, P., D. W. Chapman, R. B. Moore and R. J. Zemp (2015) Monitoring photodynamic therapy with photoacoustic microscopy. *J. Biomed. Opt.* **20**, 106012.

72. Neuschmelting, V., K. Kim, J. Malekzadeh-Najafabadi, S. Jebiwott, J. Prakash, A. Scherz, J. A. Coleman, M. F. Kircher and V. Ntziachristos (2018) WST11 vascular targeted photodynamic therapy effect monitoring by multispectral optoacoustic tomography (MSOT) in mice. *Theranostics* **8**, 723–734.

73. Mallidi, S., K. Watanabe, D. Timerman, D. Schoenfeld and T. Hasan (2015) Prediction of tumor recurrence and therapy monitoring using ultrasound-guided photoacoustic imaging. *Theranostics* **5**, 289–301.

74. Devor, A., S. Sakadzic, V. Srinivasan, M. Yaseen, K. Nizar, P. Saisan, P. Tian, A. Dale, S. Vinogradov, M. A. Franceschini and D. Boas (2012) Frontiers in optical imaging of cerebral blood flow and metabolism. *J. Cerebral Blood Flow Metab.* **32**, 1259–1276.

75. Pogue, B. W., R. D. Braun, J. L. Lanzen, C. Erickson and M. W. Dewhirst (2001) Analysis of the heterogeneity of pO2 dynamics during photodynamic therapy with verteporfin. *Photochem. Photobiol.* **74**, 700–706.

76. Shao, Q. and S. Ashkenazi (2015) Photoacoustic lifetime imaging for direct in vivo tissue oxygen monitoring. *J. Biomed. Opt.* **20**, 036004.

77. Kou, J., D. Dou and L. Yang (2017) Porphyrin photosensitizers in photodynamic therapy and its applications. *Oncotarget* **8**, 81591–81603.

78. Matsumura, Y. and H. Maeda (1986) A new concept for macromolecular therapeutics in cancer chemotherapy: mechanism of tumoritropic accumulation of proteins and the antitumor agent smancs. *Can. Res.* **46**, 6387–6392.

79. Yoo, J., C. Park, G. Yi, D. Lee and H. Koo (2019) Active targeting strategies using biological ligands for nanoparticle drug delivery systems. *Cancers (Basel)* **11**, 640.

80. Bazak, R., M. Houri, S. El Achy, S. Kamel and T. Refaat (2015) Cancer active targeting by nanoparticles: a comprehensive review of literature. *J. Cancer Res. Clin. Oncol.* **141**, 769–784.

81. Couleaud, P., V. Morosini, C. Frochot, S. Richeter, L. Raehm and J.-O. Durand (2010) Silica-based nanoparticles for photodynamic therapy applications. *Nanoscale* **2**, 1083–1095.

82. Wang, C., L. Cheng and Z. Liu (2013) Upconversion nanoparticles for photodynamic therapy and other cancer therapeutics. *Theranostics* **3**, 317–330.

83. Rai, P., S. Mallidi, X. Zheng, R. Rahmanzadeh, Y. Mir, S. Elrington, A. Khurshid and T. Hasan (2010) Development and applications of photo-triggered theranostic agents. *Adv. Drug Deliv. Rev.* **62**, 1094–1124.

84. Obaid, G., M. Broekgaarden, A.-L. Bulin, H.-C. Huang, J. Kuriakose, J. Liu and T. Hasan (2016) Photonanomedicine: a convergence of photodynamic therapy and nanotechnology. *Nanoscale* **8**, 12471–12503.

85. Madsen, H. H. T. and F. Rasmussen (2011) Contrast-enhanced ultrasound in oncology. Cancer Imaging 11 Spec No A, S167–173.

86. Cornelis, F. H., K. Kim, J. C. Durack, S. Jebiwott, A. Scherz, G. Srimathveeravalli and J. A. Coleman (2017) Contrast enhanced ultrasound imaging can predict vascular-targeted photodynamic therapy induced tumor necrosis in small animals. *Photodiagn. Photodyn. Ther.* **20**, 165–168.

87. Huynh, E., J. F. Lovell, B. L. Helfield, M. Jeon, C. Kim, D. E. Goertz, B. C. Wilson and G. Zheng (2012) Porphyrin shell microbubbles with intrinsic ultrasound and photoacoustic properties. *J. Am. Chem. Soc.* **134**, 16464–16467.

88. You, Y., X. Liang, T. Yin, M. Chen, C. Qiu, C. Gao, X. Wang, Y. Mao, E. Qu, Z. Dai and R. Zheng (2018) Porphyrin-grafted lipid microbubbles for the enhanced efficacy of photodynamic therapy in prostate cancer through ultrasound-controlled in situ accumulation. *Theranostics* **8**, 1665–1677.

89. Park, D. J., K. H. Min, H. J. Lee, K. Kim, I. C. Kwon, S. Y. Jeong and S. C. Lee (2016) Photosensitizer-loaded bubble-generating mineralized nanoparticles for ultrasound imaging and photodynamic therapy. *J. Mater. Chem B* **4**, 1219–1227.

90. Sun, S., Y. Xu, P. Fu, M. Chen, S. Sun, R. Zhao, J. Wang, X. Liang and S. Wang (2018) Ultrasound-targeted photodynamic and gene dual therapy for effectively inhibiting triple negative breast cancer by cationic porphyrin lipid microbubbles loaded with HIF1alpha-siRNA. *Nanoscale* **10**, 19945–19956.

91. Levine, M. and R. Tjian (2003) Transcription regulation and animal diversity. *Nature* **424**, 147–151.

92. Bartel, D. P. (2004) MicroRNAs: genomics, biogenesis, mechanism, and function. *Cell* **116**, 281–297.

93. Gutschner, T. and S. Diederichs (2012) The hallmarks of cancer. *RNA Biol.* **9**, 703–719.

94. Gupta, R. A., N. Shah, K. C. Wang, J. Kim, H. M. Horlings, D. J. Wong, M.-C. Tsai, T. Hung, P. Argani, J. L. Rinn, Y. Wang, P. Brzoska, B. Kong, R. Li, R. B. West, M. J. van de Vijver, S. Sukumar and H. Y. Chang (2010) Long non-coding RNA HOTAIR reprograms chromatin state to promote cancer metastasis. *Nature* **464**, 1071.

95. Morlando, M., M. Ballarino and A. Fatica (2015) Long non-coding RNAs: New players in hematopoiesis and leukemia. *Front. Med.* **2**.

96. Hoffman, D. P., G. Shtengel, C. S. Xu, K. R. Campbell, M. Freeman, L. Wang, D. E. Milkie, H. A. Pasolli, N. Iyer, J. A. Bogovic, D. R. Stabley, A. Shirinifard, S. Pang, D. Peale, K. Schaefer, W. Pomp, C.-L. Chang, J. Lippincott-Schwartz, T. Kirchhausen, D. J. Solecki, E. Betzig and H. Hess (2019) Correlative three-dimensional super-resolution and block face electron microscopy of whole vitreously frozen cells. *bioRxiv*, 773986.

97. Zhong, H., A. M. De Marzo, E. Laughner, M. Lim, D. A. Hilton, D. Zagzag, P. Buechler, W. B. Isaacs, G. L. Semenza and J. W. Simons (1999) Overexpression of hypoxia-inducible factor 1α in common human cancers and their metastases. *Can. Res.* **59**, 5830.

98. Zhang, Y., J. Yu, A. R. Kahkoska and Z. Gu (2017) Photoacoustic drug delivery. *Sensors* **17**, 1400.

99. Lin, J., S. Wang, P. Huang, Z. Wang, S. Chen, G. Niu, W. Li, J. He, D. Cui, G. Lu, X. Chen and Z. Nie (2013) Photosensitizer-loaded gold vesicles with strong plasmonic coupling effect for imaging-guided photothermal/photodynamic therapy. *ACS Nano* **7**, 5320–5329.

100. Lin, Y., Y. Wu, R. Wang, G. Tao, P. F. Luo, X. Lin, G. Huang, J. Li and H. H. Yang (2018) Two-dimensional tellurium nanosheets for photoacoustic imaging-guided photodynamic therapy. *Chem. Commun. (Camb.)* **54**, 8579–8582.

101. Ding, H., H. Cai, J. Chen, T. Lu, W. Wen, G. Nie and X. Wang (2019) Cryodesiccation-driven crystallization preparation approach for zinc(II)-phthalocyanine nanodots in cancer photodynamic therapy and photoacoustic imaging. *Mikrochim. Acta* **186**, 237.

102. Hou, M., C. Yan, Z. Chen, Q. Zhao, M. Yuan, Y. Xu and B. Zhao (2018) Multifunctional NIR-responsive poly(vinylpyrrolidone)-Cu-Sb-S nanotheranostic agent for photoacoustic imaging and photothermal/photodynamic therapy. *Acta Biomater.* **74**, 334–343.

103. Sun, P., X. Wang, G. Wang, W. Deng, Q. Shen, R. Jiang, W. Wang, Q. Fan and W. Huang (2018) A perylene diimide zwitterionic polymer for photoacoustic imaging guided photothermal/photodynamic synergistic therapy with single near-infrared irradiation. *J Mater Chem B* **6**, 3395–3403.

104. Kim, J.-Y., W. I. Choi, M. Kim and G. Tae (2013) Tumor-targeting nanogel that can function independently for both photodynamic and photothermal therapy and its synergy from the procedure of PDT followed by PTT. *J. Controlled Rel.* **171**, 113–121.

105. Chen, F., P. W. Tillberg and E. S. Boyden (2015) Expansion microscopy. *Science* **347**, 543.

106. Liou, G.-Y. and P. Storz (2010) Reactive oxygen species in cancer. *Free Radic. Res.* **44**, 479–496.

107. Gao, S., G. Wang, Z. Qin, X. Wang, G. Zhao, Q. Ma and L. Zhu (2017) Oxygen-generating hybrid nanoparticles to enhance fluorescent/photoacoustic/ultrasound imaging guided tumor photodynamic therapy. *Biomaterials* **112**, 324–335.

108. López-Lázaro, M. (2007) Dual role of hydrogen peroxide in cancer: Possible relevance to cancer chemoprevention and therapy. *Cancer Lett.* **252**, 1–8.

109. Luo, Z., M. Zheng, P. Zhao, Z. Chen, F. Siu, P. Gong, G. Gao, Z. Sheng, C. Zheng, Y. Ma and L. Cai (2016) Self-monitoring artificial red cells with sufficient oxygen supply for enhanced photodynamic therapy. *Sci. Rep.* **6**, 23393.

110. Yang, Q. and S. Lai (2015) Anti-PEG immunity: Emergence, characteristics, and unaddressed questions. *Wiley Interdisciplinary Rev.* **7**, 655–677.

111. Xia, Q., Y. Zhang, Z. Li, X. Hou and N. Feng (2019) Red blood cell membrane-camouflaged nanoparticles: a novel drug delivery system for antitumor application. *Acta Pharmaceutica Sinica B* **9**, 675–689.

112. Kim, Y. C., J. Y. Choi, Y. E. Chung, S. Bang, M. J. Kim, M. S. Park and K. W. Kim (2010) Comparison of MRI and endoscopic ultrasound in the characterization of pancreatic cystic lesions. *AJR Am. J. Roentgenol.* **195**, 947–952.

113. Fernandez-Esparrach, G., J. R. Ayuso-Colella, O. Sendino, M. Pages, M. Cuatrecasas, M. Pellise, J. Maurel, C. Ayuso-Colella, B. Gonzalez-Suarez, J. Llach, A. Castells and A. Gines (2011) EUS and magnetic resonance imaging in the staging of rectal cancer: a prospective and comparative study. *Gastrointest. Endosc.* **74**, 347–354.

114. Pinkavova, I., D. Fischerova, M. Zikan, A. Burgetova, J. Slama, J. Svarovsky, P. Dundr, L. Dusek and D. Cibula (2013) Transrectal ultrasound and magnetic resonance imaging in the evaluation of tumor size following neoadjuvant chemotherapy for locally advanced cervical cancer. *Ultrasound Obstet. Gynecol.* **42**, 705–712.

115. Lee, M. C., S. J. Gonzalez, H. Lin, X. Zhao, J. V. Kiluk, C. Laronga and B. Mooney (2015) Prospective trial of breast MRI versus 2D and 3D ultrasound for evaluation of response to neoadjuvant chemotherapy. *Ann. Surg. Oncol.* **22**, 2888–2894.

116. Spolverato, G., A. Ejaz, Y. Kim, M. H. Squires, G. A. Poultsides, R. C. Fields, C. Schmidt, S. M. Weber, K. Votanopoulos, S. K. Maithel and T. M. Pawlik (2015) Use of endoscopic ultrasound in the preoperative staging of gastric cancer: a multi-institutional study of the US gastric cancer collaborative. *J. Am. Coll. Surg.* **220**, 48–56.

117. Jaeger, M., G. Held, S. Peeters, S. Preisser, M. Grunig and M. Frenz (2015) Computed ultrasound tomography in echo mode for imaging speed of sound using pulse-echo sonography: proof of principle. *Ultrasound Med. Biol.* **41**, 235–250.

118. Sanabria, S. J., E. Ozkan, M. Rominger and O. Goksel (2018) Spatial domain reconstruction for imaging speed-of-sound with pulse-echo ultrasound: simulation and in vivo study. *Phys. Med. Biol.* **63**, 215015.

119. Wu, G.-G., L.-Q. Zhou, J.-W. Xu, J.-Y. Wang, Q. Wei, Y.-B. Deng, X.-W. Cui and C. F. Dietrich (2019) Artificial intelligence in breast ultrasound. *World J. Radiol.* **11**, 19–26.

120. Valluru, K. S. and J. K. Willmann (2016) Clinical photoacoustic imaging of cancer. *Ultrasonography* **35**, 267–280.

121. Collins, J.-A., A. Rudenski, J. Gibson, L. Howard and R. O'Driscoll (2015) Relating oxygen partial pressure, saturation and content: the haemoglobin-oxygen dissociation curve. *Breathe (Sheff)* **11**, 194–201.

122. Cao, F., Z. Qiu, H. Li and P. Lai. (2017) Photoacoustic imaging in oxygen detection. *Appl. Sci.* **7**, 1262.

123. Gerling, M., Y. Zhao, S. Nania, K. J. Norberg, C. S. Verbeke, B. Englert, R. V. Kuiper, Å. Bergström, M. Hassan, A. Neesse, J. M. Löhr and R. L. Heuchel (2014) Real-time assessment of tissue hypoxia in vivo with combined photoacoustics and high-frequency ultrasound. *Theranostics* **4**, 604–613.

124. Tomaszewski, M. R., M. Gehrung, J. Joseph, I. Quiros-Gonzalez, J. A. Disselhorst and S. E. Bohndiek (2018) Oxygen-enhanced and dynamic contrast-enhanced optoacoustic tomography provide surrogate biomarkers of tumor vascular function, hypoxia, and necrosis. *Can. Res.* **78**, 5980.

125. Fakhrejahani, E., M. Torii, T. Kitai, S. Kanao, Y. Asao, Y. Hashizume, Y. Mikami, I. Yamaga, M. Kataoka, T. Sugie, M. Takada, H. Haga, K. Togashi, T. Shiina and M. Toi (2015) Clinical report on the first prototype of a photoacoustic tomography system with dual illumination for breast cancer imaging. *PLoS ONE* **10**, e0139113.

126. Zhong, H., T. Duan, H. Lan, M. Zhou and F. Gao (2018) Review of low-cost photoacoustic sensing and imaging based on laser diode and light-emitting diode. *Sensors* **18**, 2264.

127. Li, W., C. Zheng, Z. Pan, C. Chen, D. Hu, G. Gao, S. Kang, H. Cui, P. Gong and L. Cai (2016) Smart hyaluronidase-actived theranostic micelles for dual-modal imaging guided photodynamic therapy. *Biomaterials* **101**, 10–19.

128. Hu, D., L. Zhong, M. Wang, H. Li, Y. Qu, Q. Liu, R. Han, L. Yuan, K. Shi, J. Peng and Z. Qian (2019) Perfluorocarbon-loaded and redox-activatable photosensitizing agent with oxygen supply for enhancement of fluorescence/photoacoustic imaging guided tumor photodynamic therapy. *Adv. Funct. Mater.* **29**, 1806199.

129. Cai, Y., P. Liang, Q. Tang, X. Yang, W. Si, W. Huang, Q. Zhang and X. Dong (2017) Diketopyrrolopyrrole-triphenylamine organic nanoparticles as multifunctional reagents for photoacoustic imaging-guided photodynamic/photothermal synergistic tumor therapy. *ACS Nano* **11**, 1054–1063.

130. Zhai, Y., W. Ran, J. Su, T. Lang, J. Meng, G. Wang, P. Zhang and Y. Li (2018) Traceable bioinspired nanoparticle for the treatment of metastatic breast cancer via NIR-trigged intracellular delivery of methylene blue and cisplatin. *Adv. Mater.* **30**, e1802378.

131. Sun, Y., H. Hu, N. Zhao, T. Xia, B. Yu, C. Shen and F. J. Xu (2017) Multifunctional polycationic photosensitizer conjugates with rich hydroxyl groups for versatile water-soluble photodynamic therapy nanoplatforms. *Biomaterials* **117**, 77–91.

132. Hu, W., H. Ma, B. Hou, H. Zhao, Y. Ji, R. Jiang, X. Hu, X. Lu, L. Zhang, Y. Tang, Q. Fan and W. Huang (2016) Engineering lysosome-targeting BODIPY nanoparticles for photoacoustic imaging and photodynamic therapy under near-infrared light. *ACS Appl. Mater. Interfaces.* **8**, 12039–12047.

133. Wang, Q., Y. Dai, J. Xu, J. Cai, X. Niu, L. Zhang, R. Chen, Q. Shen, W. Huang and Q. Fan (2019) All-in-one phototheranostics: single laser triggers NIR-II fluorescence/photoacoustic imaging guided photothermal/photodynamic/chemo combination therapy. *Adv. Funct. Mater.* **29**, 1901480.

134. Beziere, N. and V. Ntziachristos (2015) Optoacoustic imaging of naphthalocyanine: potential for contrast enhancement and therapy monitoring. *J. Nucl. Med.* **56**, 323–328.

135. Mauriello-Jimenez, C., M. Henry, D. Aggad, L. Raehm, X. Cattoën, M. Wong Chi Man, C. Charnay, S. Alpugan, V. Ahsen, D. K. Tarakci, P. Maillard, M. Maynadier, M. Garcia, F. Dumoulin, M. Gary-Bobo, J.-L. Coll, V. Josserand and J.-O. Durand (2017) Porphyrin- or phthalocyanine-bridged silsesquioxane nanoparticles for two-photon photodynamic therapy or photoacoustic imaging. *Nanoscale* **9**, 16622–16626.

136. Tan, X., J. Wang, X. Pang, L. Liu, Q. Sun, Q. You, F. Tan and N. Li (2016) Indocyanine green-loaded silver nanoparticle@polyaniline core/shell theranostic nanocomposites for photoacoustic/near-infrared fluorescence imaging-guided and single-light-triggered photothermal and photodynamic therapy. *ACS Appl. Mater. Interfaces.* **8**, 34991–35003.

137. Wang, G., F. Zhang, R. Tian, L. Zhang, G. Fu, L. Yang and L. Zhu (2016) Nanotubes-embedded indocyanine green-hyaluronic acid nanoparticles for photoacoustic-imaging-guided phototherapy. *ACS Appl. Mater. Interfaces.* **8**, 5608–5617.

138. Li, X., X. Wang, C. Zhao, L. Shao, J. Lu, Y. Tong, L. Chen, X. Cui, H. Sun, J. Liu, M. Li, X. Deng and Y. Wu (2019) From one to all: self-assembled theranostic nanoparticles for tumor-targeted imaging and programmed photoactive therapy. *J. Nanobiotechnol.* **17**, 23.

139. Yang, Q., H. Jin, Y. Gao, J. Lin, H. Yang and S. Yang (2019) Photostable iridium(III)–cyanine complex nanoparticles for photoacoustic imaging guided near-infrared photodynamic therapy in vivo. *ACS Appl. Mater. Interfaces.* **11**, 15417–15425.

140. Ma, J., D. Chen, Y. Li, Y. Chen, Q. Liu, X. Zhou, K. Qian, Z. Li, H. Ruan, Z. Hou and X. Zhu (2018) Zinc phthalocyanine-soybean phospholipid complex based drug carrier for switchable photoacoustic/fluorescence image, multiphase photothermal/photodynamic treatment and synergetic therapy. *J. Control. Rel.* **284**, 1–14.

141. Bharathiraja, S., P. Manivasagan, Y. O. Oh, M. S. Moorthy, H. Seo, N. Q. Bui and J. Oh (2017) Astaxanthin conjugated polypyrrole nanoparticles as a multimodal agent for photo-based therapy and imaging. *Int. J. Pharm.* **517**, 216–225.

AUTHOR BIOGRAPHIES

Scott C. Hester graduated with a Bachelor of Science in Biology from George Mason University, Fairfax, VA. He attended the Foundation for Advanced Education in the Sciences Graduate School at National Institutes of Health and is currently pursuing a Master's Degree in Biology, Bioengineering and Nanotechnology from the Harvard Extension School. Mr. Hester's interests lie in the fields of super-resolution microscopy, photodynamic and sonodynamic therapies, stem cell and RNA biology, BioMEMS, and epigenetics.

Maju Kuriakose received his Ph.D. in Physics (Thermal characterization of Materials) from the University of Littoral Opal Coast in Dunkerque, France. Thereafter, he worked as a postdoctoral fellow at the University of Maine in Le Mans, France, in picosecond laser ultrasonics to mechanically characterize materials under extreme conditions. From 2017 (University of Bern, Switzerland), he worked on developing speed of sound methods for biomedical imaging using clinical echo ultrasound. Dr. Kuriakose is now a postdoctoral fellow in the integrated Biofunctional Imaging and Therapeutics Laboratory at the Department of Biomedical Engineering at Tufts University and is working on developing a clinically translatable photoacoustic system.
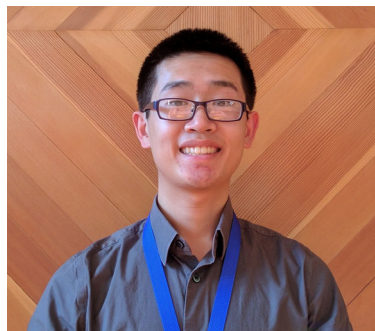
Christopher D. Nguyen received his Bachelor's and Master's Degree in Optical Sciences and Engineering from the University of Arizona. He was the recipient of several awards including the Wildcat Excellence Award, Thorlabs Photonics Is the Future Award and the James Mayo Family Graduate Student Scholarship in Optical Sciences. He is currently pursuing his Ph.D. in the Department of Biomedical Engineering at Tufts University.

Srivalleesha Mallidi received her Master's and Ph.D. Degree in Biomedical Engineering from the University of Texas at Austin. Her graduate work was on molecular specific photoacoustic imaging to understand nanomolecular interactions. She received New Investigator Award from the Central Texas Clinical Research Forum for this work. After graduation, she joined Wellman Center for Photomedicine at Massachusetts General Hospital (MGH), Harvard Medical School with a goal to translate the imaging techniques to clinic, and was a NIH Ruth L. Kirschstein postdoctoral fellow. She won several awards during her postdoctoral tenure at MGH including the Young Investigator Award at the Frontiers in Biomedical Imaging Science Symposium held at Vanderbilt University. She was also awarded the American Society of Lasers in Medicine and Surgery Research Award for junior faculty. Currently, Dr. Mallidi is Assistant Professor at the Department of Biomedical Engineering at Tufts University, Medford, MA, and she directs the integrated Biofunctional Imaging Laboratory that focuses on ultrasound- and photoacoustic imaging-based therapeutic strategies.